



Structural Transition from Helices to Hemihelices

Jia Liu¹*, Jiangshui Huang¹*, Tianxiang Su¹, Katia Bertoldi^{1,2*}, David R. Clarke^{1,2*}

1 School of Engineering and Applied Sciences, Harvard University, Cambridge, Massachusetts, United States of America, **2** Kavli Institute, Harvard University, Cambridge, Massachusetts, United States of America

Abstract

Helices are amongst the most common structures in nature and in some cases, such as tethered plant tendrils, a more complex but related shape, the hemihelix forms. In its simplest form it consists of two helices of opposite chirality joined by a perversion. A recent, simple experiment using elastomer strips reveals that hemihelices with multiple reversals of chirality can also occur, a richness not anticipated by existing analyses. Here, we show through analysis and experiments that the transition from a helical to a hemihelical shape, as well as the number of perversions, depends on the height to width ratio of the strip's cross-section. Our findings provides the basis for the deterministic manufacture of a variety of complex three-dimensional shapes from flat strips.

Citation: Liu J, Huang J, Su T, Bertoldi K, Clarke DR (2014) Structural Transition from Helices to Hemihelices. PLoS ONE 9(4): e93183. doi:10.1371/journal.pone.0093183

Editor: Markus J. Buehler, Massachusetts Institute of Technology, United States of America

Received: October 30, 2013; **Accepted:** March 3, 2014; **Published:** April 23, 2014

Copyright: © 2014 Liu et al. This is an open-access article distributed under the terms of the Creative Commons Attribution License, which permits unrestricted use, distribution, and reproduction in any medium, provided the original author and source are credited.

Funding: This work was supported by the Materials Research Science and Engineering Center under NSF Award No. DMR-0820484. K.B. also acknowledges support from the National Science Foundation (CMMI-1149456-CAREER) and the Wyss institute through the Seed Grant Program. D.R. acknowledges funding from the National Science Foundation (CMMI-1333835). The funders had no role in study design, data collection and analysis, decision to publish, or preparation of the manuscript.

Competing Interests: The authors have declared that no competing interests exist.

* E-mail: bertoldi@seas.harvard.edu (KB); clarke@seas.harvard.edu (DRC)

† These authors contributed equally to this work.

Introduction

Nature abounds with complex, three-dimensional shapes [1,2]. Of these, the helix and spiral are amongst the most ubiquitous, often emerging during growth from initially straight or flat 2-D configurations. For instance, initially straight roots form helical shapes while attempting to penetrate more compact soils [3]. Similarly, as seed pods open, a chirality-creating mechanism turns an initially flat pod valve into a helix [4–6]. In other instances, the chirality can switch during growth as noted by Asa Gray [7] and Darwin [8] in their studies of plant tendrils. They noted that as a growing plant tendril circumnates it can attach to another object and then, being fixed at both ends, its chirality reverses in between to maintain its topology as it continues to grow [9,10]. This reversal of chirality - often referred to as a perversion - forms what we term here a simple hemihelix. More generally, we introduce the term hemihelix to describe multiple reversals in chirality connected by perversions. As pointed out by McMillen and Goriely [9], perversions have been observed in several physical systems with a literature that dates back to Ampère's letter to the French Academy of Sciences. Subsequently, the word perversion was used by J.B. Listing to describe the inversion of chirality in seashells [11] and by Maxwell in the context of light propagating in magnetic materials [12], but only recently have Goriely and Tabor rigorously defined perversions [13]. Although perversions can also be introduced manually, for instance, by the simple operation of holding one end of a helical telephone cord fixed and twisting the other in a direction counter to its initial chirality, perversions occur in nature during growth and as illustrated by the example of the attached plant tendril a single perversion forms. Interestingly, wool fibres can also form hemihelices with distributions of perversions separating alternating helical sections of

opposite chiralities [14]. Recently, similar three-dimensional shapes with multiple perversions have been created by joining two strips of elastomers of different lengths [15]. Moreover, rippled patterns with periodic distributions of perversions have also been discerned along the peripheries of thin sheets, such as the edge of the gut [16] and the edges of flowers and leaves [17–21]. These observations raise two fundamental questions: (i) what controls whether a helix or a hemihelix forms? and (ii) what determines the number of perversions that will form?

In this work we address these two questions using a combination of experiments, numerical simulations and analyses. These show that the formation of both helices and hemihelices with periodic distributions of perversions can be fully understood in terms of competing buckling instabilities that depend on the aspect ratio of the cross-section of the bi-strip. Experiments indicate that there is a well-defined phase transition between the helix and the hemihelix and this is confirmed by an analysis based on Kirchhoff's rod theory. Our analysis also shows how the number of perversions depends on the cross-sectional aspect ratio, confirming the experimental findings discussed below and shown in Fig. 1 and those represented later on a phase diagram.

Experimental Observations

Our observations come from a series of experiments in which two long strips of elastomer are stretched, joined and then released. The sequence of operations is shown in Fig. 2. We start with two strips of the same material (dyed to distinguish them) of the same initial width w but unequal length. The short, red strip, with length L' and height h' , is stretched uniaxially to be equal in length to the longer, blue strip, length L and height h . The initial heights are chosen so that after stretching the bi-strip system has a

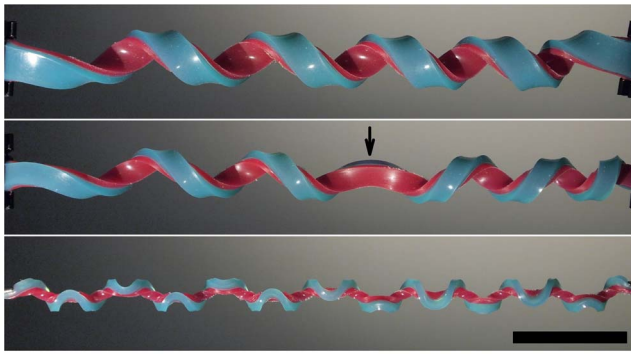


Figure 1. Illustration of a helix (top), a hemihelix with one perversion marked by an arrow (middle) and a hemihelix with multiple perversions (bottom). The scale bar is 5 cm, and is the same for each image. These different shapes were all produced in the same way as shown in figure 2 with the same value of pre-strain $\chi = 1.5$ but with decreasing values of the height-to-width ratio of the bi-strip's cross-section. $L = 50\text{ cm}$, $w = 3\text{ mm}$, $h = 12, 8, 2.5\text{ mm}$. doi:10.1371/journal.pone.0093183.g001

rectangular cross-section. The two strips are then glued together side-by-side along their length. At this stage, the bi-strips are flat and the red strip is under a uniaxial pre-strain, defined as $\chi = (L - L')/L'$. Being elastomers, volume conservation requires that the heights are related by $h' = h\sqrt{1 + \chi}$. Then, in the final operation, the force stretching the ends of the bi-strip is gradually released, with the ends free to rotate. More details of the manufacturing and experimental procedures are given in *Materials and Methods*.

Upon release, the initially flat bistrips start to bend and twist out of plane and evolve towards either a helical or hemihelical shape, depending on the cross-sectional aspect ratio. As indicated by the images in Fig. 1, when the aspect ratio h/w is small, we observe the formation of periodic perversions, separating helical segments of alternating chiralities, whereas when the bi-strips have a large aspect ratio, they spontaneously twist along their length to form a regular helix. Significantly, these three-dimensional shapes form spontaneously and do so irrespective of whether the release is abrupt or the ends are slowly brought together. Furthermore, it is also observed that after release, the bi-strip can be stretched

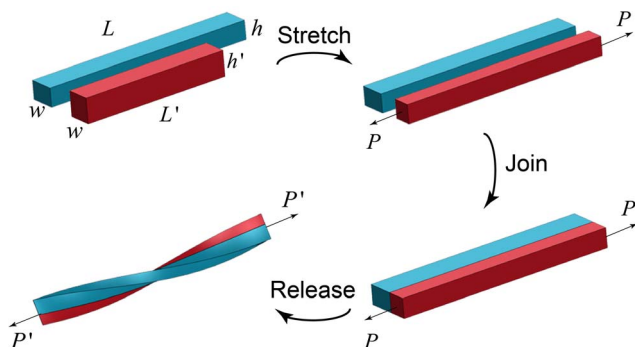


Figure 2. Sequence of operations leading to the spontaneous creation of hemihelices and helices. Starting with two long elastomer strips of different lengths, the shorter one is stretched to be the same length as the other. While the stretching force, P , is maintained, the two strips are joined side-by-side. Then, as the force is slowly released, the bi-strip twists and bends to create either a helix or a hemihelix. doi:10.1371/journal.pone.0093183.g002

straight again and released many times and each time the same shape, complete with the same number of perversions, reforms. Experiments were also performed under water to minimize gravitational effects and dampen vibrations. Video recordings, reproduced in File S1, capture the evolution of the 3D shapes, several transient features including how perversions move along the bi-strip to form a regular arrangement as well as how an initial twisting motion is reversed.

The experimental observations indicate that the number of perversions n is the critical geometric parameter that distinguishes which shape forms upon release. Assuming that the perversions are uniformly distributed along the length of the bi-strip, the number that form can be expected to depend on the prestrain ratio, the cross-sectional aspect ratio and the length of the bi-strip. Dimensional arguments then suggest that the number is given by: $wn/L = g(\chi, h/w)$. To establish how the number of perversions depends on these variables, a series of experiments were performed with different values of pre-strain and cross-sectional aspect ratio. The results of these experiments are shown in the structural phase diagram in Fig. 3 where the numbers associated with the symbols indicate the number of perversions observed. The boundary between the formation of helices and hemihelices is shown shaded. The data in Fig. 3 indicates that increasing the h/w ratio drives the strip from the hemihelical configurations to helices. On the other hand, the prestrain ratio χ has only a weak influence on both the helix-to-hemihelix transition and the number of perversions. This phase diagram (Fig. 3) was established under experimental conditions that allowed both ends to freely rotate as the stretching force was reduced. A similar phase diagram (Fig. S5 in File S1) but notable by the absence of any helices was obtained upon unloading when the ends were constrained from rotating (see File S1 for details).

Finite element simulations

Numerical simulations to explore the morphological changes occurring during the release in the bi-strip system were conducted using detailed dynamic finite element simulations. In our analysis,

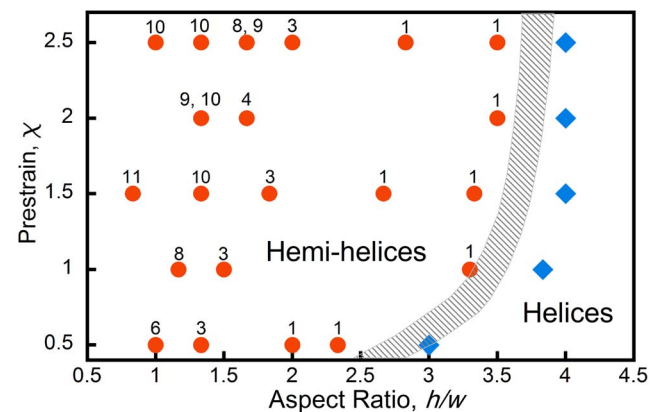


Figure 3. The number of perversions observed as a function of both the prestrain and the cross-section aspect ratio, h/w . The data indicates that there is a transition between the formation of helices at larger aspect ratios and hemihelices at smaller aspect ratios. The precise phase boundary cannot be determined with any precision experimentally and so is shown shaded but there is evidently only a weak dependence on the value of the pre-strain. In some cases, bistrips made the same way produce either one or the other of the two perversion numbers indicated. doi:10.1371/journal.pone.0093183.g003

the non-linear response of the elastomer was captured using a hyperelastic Gent model [22]. 3D models of the bi-strip system were built and the prestretch effect was modeled by decomposition of the deformation gradient, $\mathbf{F} = \mathbf{F}^L \mathbf{F}^P$, where \mathbf{F}^L is the loading induced gradient while \mathbf{F}^P is the prestretch induced gradient, $\mathbf{F}^P = \text{diag}(\chi + 1, 1/\sqrt{\chi + 1}, 1/\sqrt{\chi + 1})$ [15]. More details of the FE simulations are given in *Materials and Methods* and File S1. These fully reproduced the experimental observations. For instance, snapshots recorded at three successive stages in the release of bi-strips having three different cross-sectional aspect ratios are shown in Fig. 4. Clearly, the simulations correctly capture the principal features observed in the experiments including the formation of perversions as well as the detailed evolution of the hemihelix and the helix as unloading occurs.

Analytical Model

To understand the origin of the experimental and numerical results reported above, we analyze the deformation of the bi-strip system modeled as a homogeneous rod with a rectangular cross section h by $2w$ (see Fig. 5) and study its behavior using Kirchhoff rod theory [23–27]. Due to the pre-stretch, the equivalent homogeneous rod has a natural curvature K and a undeformed contour length L_* when no external forces and moments are applied (see Fig. S8 in File S1). Both K and L_* can be related to χ , w and L from the bi-strip system (see File S1 for details)

$$K = \frac{1}{w} \frac{12\chi}{8(\chi+2)}, \quad L_* = L \frac{8(\chi+2)}{\chi^2 + 16\chi + 16}. \quad (1)$$

The rod is then represented by a space curve $\mathbf{x}(s, t)$, whose position depends on the arc length s and time t (see Fig. 5). In addition, to characterize the deformation of the rod an orthonormal local director basis $(\mathbf{d}_1, \mathbf{d}_2, \mathbf{d}_3) = (\mathbf{d}_1(s, t), \mathbf{d}_2(s, t), \mathbf{d}_3(s, t))$ is introduced, where \mathbf{d}_3 is identified as the tangent vector and \mathbf{d}_1 and \mathbf{d}_2 lie along the principal directions of the cross-section (Fig. 5). The condition of orthonormality implies the existence of a twist vector

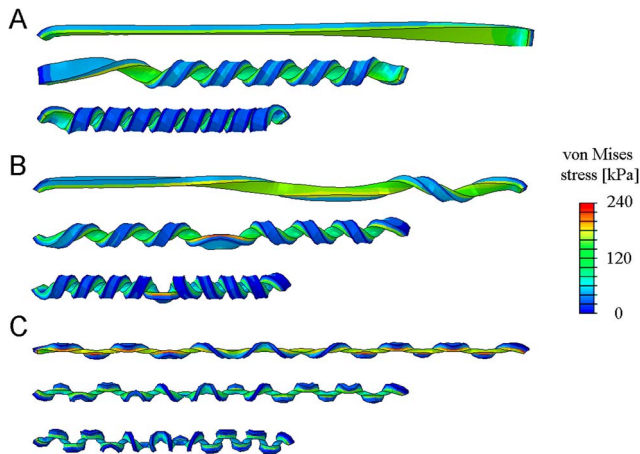


Figure 4. Snapshots recorded from the finite element simulations, illustrating the formation of (A) a helix, (B) a hemihelix with single perversion and (C) a hemihelix with 12 perversions. The colors represent the local values of the computed von Mises stress. The prestrain $\chi = 1.5$ was the same in all three cases. $L = 50 \text{ cm}$, $w = 3 \text{ mm}$, (A) $h = 2.5 \text{ mm}$, (B) $h = 8 \text{ mm}$, (C) $h = 12 \text{ mm}$. The images are taken when the end to end distances are 35 cm , 26 cm , 18 cm . Gravity was included in the simulations and acts from left to right in these images. doi:10.1371/journal.pone.0093183.g004

$\boldsymbol{\kappa} = \kappa_1 \mathbf{d}_1 + \kappa_2 \mathbf{d}_2 + \kappa_3 \mathbf{d}_3$ satisfying

$$\mathbf{d}_i' = \boldsymbol{\kappa} \times \mathbf{d}_i, \quad i = 1, 2, 3 \quad (2)$$

where $(\cdot)' = \partial(\cdot)/\partial s$, κ_1 and κ_2 are the material curvature and κ_3 is the twist density.

Balance of force and angular momentum gives

$$\begin{aligned} \mathbf{F}' &= \rho A \ddot{\mathbf{d}}_3 \\ \mathbf{M}' + \mathbf{d}_3 \times \mathbf{F} &= \rho (I_2 \mathbf{d}_1 \times \ddot{\mathbf{d}}_1 + I_1 \mathbf{d}_2 \times \ddot{\mathbf{d}}_2) \end{aligned} \quad (3)$$

where $(\dot{\cdot}) = \partial(\cdot)/\partial t$, \mathbf{F} and \mathbf{M} are the resultant force and moment acting on the cross section, ρ is the mass per unit volume of the rod, $A = 2wh$ is the cross-sectional area and $I_1 = (2w)^3 h / 12$ and $I_2 = 2wh^3 / 12$ are the principal moments of inertial of the cross section.

Finally, to facilitate the analysis, the material is taken to be linear elastic, so that

$$\mathbf{M} = EI_1(\kappa_1 - K)\mathbf{d}_1 + EI_2\kappa_2\mathbf{d}_2 + GJ\kappa_3\mathbf{d}_3, \quad (4)$$

where E is the Young's modulus, G is the shear modulus, K describes the local non-vanishing intrinsic curvature and is given by Eqn. (1). Moreover, J is the torsion constant, which for a rectangular cross-section can be approximated as $J \approx ab^3 [1/3 - 0.21b/a(1 - (b/a)^4)]$ [28], where $a = \max(2w, h)$ and $b = \min(2w, h)$.

Stability Analysis

Our starting point is a fully stretched rod under applied tension $\mathbf{F} = F_1 \mathbf{d}_1 + F_2 \mathbf{d}_2 + F_3 \mathbf{d}_3 = P \mathbf{d}_3$. Since our experimental observations clearly show that at a critical point during the release the straight configuration becomes unstable and the rod evolves into complex 3D shapes (see videos in SI), we investigate the stability of the system during unloading. We first analyze the transition from straight to helical configurations and then the formation of hemihelices with periodic distributions of perversions. Finally, we will show that at the onset of bifurcation a helix can be described as a hemihelix with a vanishing number of perversions.

Transition from straight to helical configurations. A helical configuration with curvature κ and torsion τ is defined by the position vector

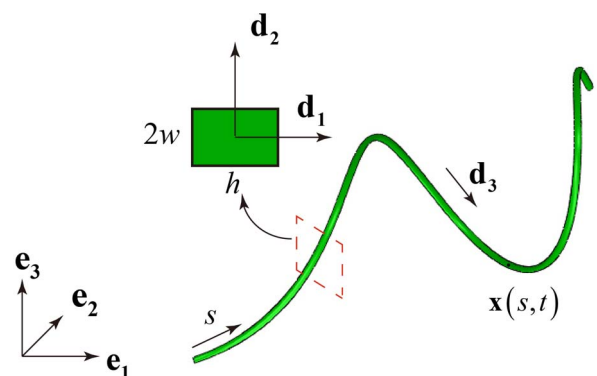


Figure 5. Coordinate system used in the Kirchhoff analysis together with the dimensions h and w of the cross-section. doi:10.1371/journal.pone.0093183.g005

$$\mathbf{x} = \frac{\kappa}{\gamma^2} \sin(\gamma s) \mathbf{e}_1 + \frac{\kappa}{\gamma^2} (\cos(\gamma s) - 1) \mathbf{e}_2 + \frac{\tau}{\gamma} s \mathbf{e}_3, \quad (5)$$

where $\gamma = \sqrt{\tau^2 + \kappa^2}$ and \mathbf{e}_i denote the global coordinate frame. To evaluate the evolution of κ and τ as a function of the applied force P , we minimize the total energy density (energy per unit length) of the helix

$$\mathcal{E} = \frac{1}{2} EI_1 (\kappa - K)^2 + \frac{1}{2} GJ \tau^2 - \frac{P}{L_*} \frac{\tau L_*}{\gamma}, \quad (6)$$

where the first, second and third term are the bending energy, twisting energy and force potential, respectively. The energy minimization criterion requires that $\partial \mathcal{E} / \partial \kappa = 0$ and $\partial \mathcal{E} / \partial \tau = 0$, which can be solved to obtain κ and τ as a function of the applied force P . It is easy to show (see File S1 for details) that they admit real, positive solutions κ and τ only if

$$P \leq P_{cr}^{helix} = \frac{(EI_1 K)^2}{GJ}. \quad (7)$$

Thus, our analysis predicts the formation of helical configurations during release when $P < P_{cr}^{helix}$.

Transition from straight to hemihelical configurations. For the case of small aspect ratios h/w , the formation of hemihelices with multiple reversal of chirality is observed in the experiments during release. These complex 3D shapes can be captured by studying perturbed states of the systems in a small neighborhood of the straight configuration [13,29,30] (see File S1 for details). This can be systematically implemented by expanding the relevant variables \mathbf{d}_i and F_i as power series in a small perturbation parameter ϵ

$$\begin{aligned} \mathbf{d}_i &= \mathbf{d}_i^{(0)} + \epsilon \mathbf{d}_i^{(1)} + \epsilon^2 \mathbf{d}_i^{(2)} + \dots \quad i=1,2,3 \\ F_i &= F_i^{(0)} + \epsilon F_i^{(1)} + \epsilon^2 F_i^{(2)} + \dots \end{aligned} \quad (8)$$

Substituting Eqns. (8) into (3), the Kirchhoff equations to the i -th order (ϵ^i) can be obtained (see File S1 for details). The first order solution is then assumed to take the form $\mathbf{c} \exp(i\omega_n s)$, where c is the amplitude vector and $\omega_n = n\pi s/L_*$ represents the angular frequency of the mode. Assuming there are no constraints on the rotation or displacement at both ends, we find that when the applied force P is decreased to

$$P_{cr}^{hemi} = \frac{(EI_1 K)^2}{GJ} - EI_2 \omega_n^2, \quad (9)$$

a non-trivial solution to the first order equations exists. Therefore, for $P < P_{cr}^{hemi}$ the straight configuration is unstable and complex 3D configurations are expected to grow and dominate. The shape of the modes may be obtained by solving the 2-nd order equilibrium equations, yielding

$$\mathbf{x} = \begin{pmatrix} -\frac{GJX_n \sin(\omega_n s)}{EI_1 K} \\ \frac{G^2 J^2 (2EI_1 + EI_2 - GJ) X_n^2 \omega_n^2 (\cos(2\omega_n s) - 1)}{2E^3 I_1^3 K^3 + 2E^2 G I_1 (4I_1 - I_2) J K \omega_n^2} \\ s - \frac{G^2 J^2 X_n^2 \omega_n \sin(2\omega_n s)}{4E^2 I_1^2 K^2} \end{pmatrix}, \quad (10)$$

where X_n is the mode amplitude.

The modes obtained from Eqns. 10 with $n=0.5, 1, 4, 7$ are shown in Fig. 6. Note that modes with $n < 1$ are included because the two ends of the bi-strip are allowed to rotate freely in the experiments. The modes with $n > 1$ clearly resemble the hemihelices observed in the experiments and consist of multiple, periodic and alternating helical sections of opposite chiralities, separated by n perversions. However, for $n < 1$ the perversion lies outside the rod, so that the system deforms into a single helical segment, leading to the formation of an helix. This is also confirmed by the fact that P_{cr}^{hemi} approaches P_{cr}^{heli} as $n \rightarrow 0$. Therefore, $n=1$ defines the boundary between forming hemihelices and helices.

In Fig. 6 we also report the evolution of the critical loads the critical loads P_{cr}^{helix} and P_{cr}^{hemi} as a function of h/w for different modes. The results clearly show that the helix is always the first to be excited. However, it is important to note that for small values of h/w the modes are very closely spaced, while as h/w increases, the critical values for different modes become more and more separated. Therefore, for high aspect ratio bistrisps, helices are more likely to form and dominate, since they evolve before hemihelical modes are triggered. In contrast, for low values of h/w we do not expect to observe helices, since multiple modes are triggered almost simultaneously.

Mode selection

In this section, we determine which mode grows to dominate the shape evolution during the release process. Since the stability analysis above indicates that several competing modes could form almost simultaneously for low values of h/w , we expect not only geometric non-linearities, but also the interactions between different modes to play a role in the mode selection process, making a rigorous mathematical analysis intractable.

For this reason and to capture the instability beyond its onset we make the ad-hoc assumption that it is the fastest growing perturbation mode at the onset of the instability that will dominate the shape evolution. Although this approach neglects the contribution of geometric non-linearities and possible interactions between different modes, it has already been successfully used not only to determine the mode selected by slender rods [29,31,32] under a number of different loading conditions, but also to identify

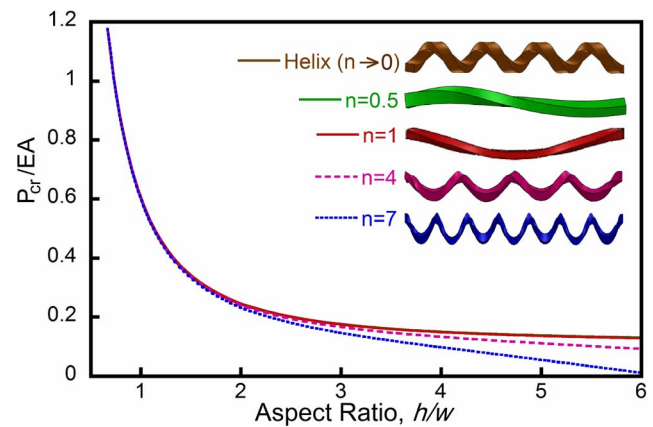


Figure 6. The critical loads for different buckling modes. For a small h/w ratio, the critical end-to-end distances r for different modes are very close to one another and difficult to distinguish. Increasing the aspect ratio by increasing the thickness decreases the critical buckling load as well as separating the individual modes. To illustrate this behavior results for four modes and the helix are shown. doi:10.1371/journal.pone.0093183.g006

the spatial fluctuations that will grow in theories of phase separation, for instance [33]. Moreover, we will show that the predictions obtained using this simple analysis nicely agree with both our experimental and numerical results.

Specifically, we assume that perturbations in the shape take the form $\mathbf{c} \exp(\sigma t + i\omega_n s)$ [13,30,34–36], where σ represents the growth rate of the mode (see File S1 for details). We then calculate the growth rate σ for a given value of P and ω_n by substituting the solution into the Kirchhoff equations to the first order. When $P < P_{cr}^{hemi}$ solutions with positive real values of σ are found, identifying those perturbations that grow exponentially with time. We expect the mode with the highest growth rate σ to dominate the shape evolution and to be the one observed in the experiments. In contrast, for $P > P_{cr}^{hemi}$ solutions with imaginary or negative σ are obtained; these will be of the order of the perturbation itself, cannot grow and hence will not be observed. Finally, when $P = P_{cr}^{hemi}$ we find that $\sigma = 0$ and the solution reduces to the one determined analytically in the stability analysis above.

In Fig. 7 we show the growth rate as a function of the mode number n for strips with different aspect ratios h/w . The results clearly show that the fastest growing mode in a strip with $h/w = 1$ is characterized by $n = 9$. In contrast, for a higher aspect ratio strip with $h/w = 2$ the mode with $n = 3$ is the fastest to evolve and is expected to dominate. Finally, if h/w further increases, the growth rate is maximum for $n < 1$, so that the formation of a helix is expected. These analytical predictions are fully consistent with the experimental results shown in Fig. 3, where it is clearly shown that the mode number monotonically decreases as a function of h/w .

Next we identify the boundary delineating the formation of hemihelices and helices. We find the mode n that has the maximum growth rate for rods characterized by different values of prestrain χ and cross-sectional aspect ratio h/w . The results are reported in Fig. 8 as contour map. The dashed lines indicate the values of n for which the growth rate is maximum and therefore corresponds to the expected number of perversions n_p . This parametric study reveals that the number of perversions in the rod after bifurcation is only moderately affected by the pre-strain χ , while the aspect ratio h/w is found to have a significant effect, again consistent with experiment. In particular, the red line in the plot marks the configurations for which $n_p = 1$. As highlighted above, if $n_p < 1$ the perversion lies outside the ends of the rod, so that the system deforms into a single helical segment and the

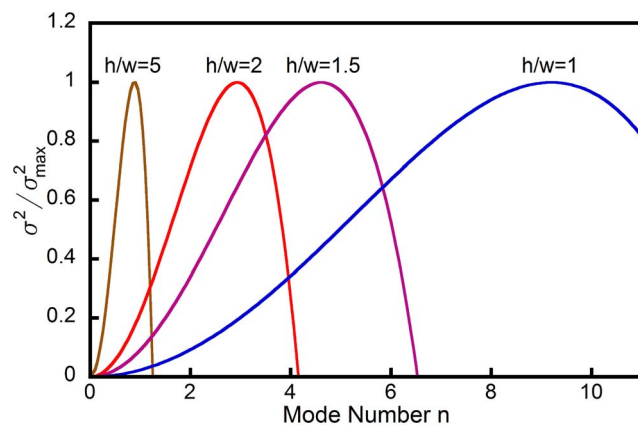


Figure 7. Growth rate σ as a function of the mode number n for three different strips characterized by $h/w = 5, 2, 1.5, 1$, $w = 3\text{mm}$, $\chi = 1.5$ and $L = 500\text{mm}$. The growth rate is determined when the applied force decreases to $P = 0.981P_{cr}^{hemi}$.
doi:10.1371/journal.pone.0093183.g007

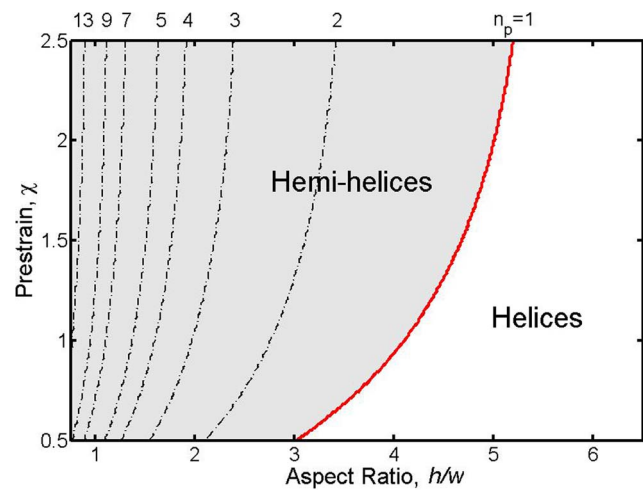


Figure 8. Contour plots showing the value of n for which the growth rate is maximum as function to χ and h/w . The growth rates are calculated for $P = 0.981P_{cr}$. Black dotted lines show the boundaries between modes with different number of perversions n_p , while the red line corresponds to $n_p = 1$ and separates hemihelices (on its left) from helices (on its right). For clarity not all the higher modes are shown.
doi:10.1371/journal.pone.0093183.g008

formation of helices is expected during the release process. Therefore, the red line defines the geometric transition between hemihelices and helices and the shaded region indicates where hemihelices form.

Conclusions

Our experimental and modeling studies show that there is a well defined structural transition between the formation of a helix and a hemihelix. The helix is energetically preferred over the straight rod as the load stretching a rod is reduced (see Fig. S10 in File S1), but other buckling mode instabilities associated with twisting can intervene preventing the shape evolution from following the lowest energy path [15]. Instead, these instability modes result in the formation of hemihelices with multiple perversions even though their total energies are higher than the simple helix [9,13,15]. We find that the growth of the buckling mode instabilities depends principally on the aspect ratio of the rod cross-section with the fastest growing mode determining the number of perversions formed. Rods with a high-aspect ratio are less susceptible to twisting instabilities and so form helices. The perversions once formed are trapped in higher energy states and can only be removed by the application of an external set of forces, for instance rotating one end with respect to the other. Additional perversions can also be introduced by counter-rotation of the ends as is common experience with winding and unwinding telephone cords.

Our analysis correctly captures both the trend of perversion number with aspect ratio as well as the hemihelix to helix transition as represented on the phase diagram of Fig. 8 and found experimentally Fig. 3. The fact that the same geometrical features are predicted to form in either linear or nonlinear elastic materials, as borne out by finite element simulations [15], indicates that while the actual number of perversions may differ and the transition from the hemihelix to helix may occur at a somewhat different aspect ratio for different materials (see Fig. S9 in File S1), the formation of hemihelices is not dependent on the material having a specific constitutive deformation behavior. It is essential, though, that the material be capable of large strains without

failing. Indeed, it is highly probable that the reason hemihelices with multiple perversions have escaped notice in the past has been that most man-made materials, unlike elastomers, would fracture well before these strains could be achieved.

We note from finite element simulations in our earlier work [15] that perversions have an elastic self-energy. This leads to the perversions repelling one another and adopting a regular spacing. Indeed, observations of the stretched bi-strip upon release, some of which are shown in videos in the supplemental information, reveal complex transients associated with the perversions. These include re-adjustment of their positions during release as well as the initial formation of a single perversion at one end that then moves along the bi-strip to the other end where it vanishes.

In a wider context, the emergence of intricate and well controlled patterns in natural slender structures, such as flowers or leaves, is often the result of specific mechanical instabilities. However, at present, our understanding of how in-plane stresses generated by nonuniform growth lead to such 3D complex shapes is incomplete. Furthermore, there is a need for translating these rules into simple strategies to engineer flat systems that shape themselves into desired 3D configurations. Indeed, the original motivation for this work was to understand which 3D shapes could be produced from flat elastic strips using one particular set of simple stretching and joining operations. Much to our surprise, we discovered that a wide range of possible shapes can be attained in our simple stressed system, specifically hemihelices with multiple chirality-reversing perversions formed under certain conditions rather than the simple helix we had expected. In summary, this work has shown, experimentally and through analysis, that by carefully controlling the cross-sectional aspect ratio and the pre-strain, it is possible to form a helix or a hemihelix with a prescribed number of perversions. We believe that our findings hold promise for fully deterministic manufacture of three-dimensional objects from pre-strained flat parts.

Materials and Methods

Materials

The elastomer strips were cut from silicone rubber sheets formed by casting a two-part commercial product (Dragon Skin 10 Slow, Reynolds Advanced Materials), between two large parallel acrylic sheets (20×60 cm) held 3 mm apart. Coloring agents (Silicone pigment, Reynolds Advanced Materials) were added before mixing. After curing for 7 hours at room temperature, the top acrylic sheet was peeled away and then the strips were cut to the desired width using a blade and peeled away from the bottom acrylic sheet. The glue was also a silicone rubber product (Sil-Poxy, Reynolds Advanced Materials).

Unloading procedure

The experimental observations of the unloading of the bi-strip were made under axial loading and free-rotation conditions. This was achieved by attaching the bi-strips between two thin nylon fibers, one attached to a fixed frame and the other to a weighted container free to rotate (Fig. S1 in File S1). The container, which had a small hole in the bottom, was filled with small metal balls to stretch the bistrup. As the metal balls ran out of the hole in the container, the gravitational force on the bi-strip steadily decreased and the deformation of the bistrup was recorded (Videos S1, S2, and S3, Figs. S2, S3, and S4 in File S1). Similar experiments but with neither end permitted to rotate (Videos S4, S5, and S6) and only one end permitted to rotate (Video S7, Fig. S6 in File S1)

were also performed. Unloading experiments were also performed under water to dampen vibrations and oscillations (Video S8).

Simulations

The commercial FE software Abaqus FEA was used for the analysis, employing the the Abaqus/Explicit solver. Three-dimensional models were built using 3D linear reduced integration elements (ABAQUS element type C3D8R). The accuracy of each mesh was ascertained through a mesh refinement study. Dynamic explicit simulations were performed and quasi-static conditions were ensured by monitoring the kinetic energy and introducing a small damping factor. The analysis were performed under force control. The material model was implemented into Abaqus/Explicit through user defined subroutine VUMAT. The material response was captured using the hyper-elastic Gent model [22]. More details on the FE simulations are provided in the File S1.

Supporting Information

File S1 Details for experimental set-up, finite element simulations and analytical model. This file also contains Figures S1–S16.

(PDF)

Video S1 Video recording for a hemihelix with multiple perversions. Both ends are free to rotate.

(WMV)

Video S2 Video recording for a hemihelix with only one perversion. Both ends are free to rotate.

(WMV)

Video S3 Video recording for a helix. Both ends are free to rotate.

(WMV)

Video S4 Video recording for a hemihelix with multiple perversions. Neither end is free to rotate. The geometry and prestretch are the same as those in Video S1.

(WMV)

Video S5 Video recording for a hemihelix with two perversions. Neither end is free to rotate. The geometry and prestretch are the same as those in Video S2.

(WMV)

Video S6 Video recording for a hemihelix with one perversion. Neither end is free to rotate. The geometry and prestretch are the same as those in Video S3.

(WMV)

Video S7 Video recording for a helix. One end is free to rotate while the other is fixed. The geometry and prestretch are the same as those in Video S3.

(WMV)

Video S8 Video recording for a hemihelix with one perversion under water. Both ends are free to rotate. The geometry and prestretch are the same as those in Video S2.

(WMV)

Author Contributions

Conceived and designed the experiments: JL JH KB DC. Performed the experiments: JH. Analyzed the data: JL JH TS KB DC. Contributed reagents/materials/analysis tools: JL JH KB DC. Wrote the paper: JL JH KB DC.

References

1. Thompson D (1942) On Growth and Form. *Courier Dover Publications*.
2. Ball P (1999) The Self-Made Tapestry. *Oxford University*.
3. Silverberg JL, Noar RD, Packer MS, Harrison MJ, Henley CL, et al. (2012) 3D imaging and mechanical modeling of helical buckling in *Medicago truncatula* plant roots. *Proc Natl Acad Sci* 109 (42): 16794–16799.
4. Forterre Y, Dumais J (2011) Generating helices in nature. *Science* 333: 1715–1716.
5. Armon S, Efrati E, Kupferman R, Sharon E (2011) Geometry and mechanics in the opening of chiral seed pods. *Science* 333: 1726–1729.
6. Chen Z, Majidi C, Srolovitz DJ, Haataja M (2011) Tunable helical ribbons. *Appl Phys Lett* 98: 011906.
7. Gray A, Sprague I (1868) *Gray's Lessons in Botany and Vegetable Physiology*. Ivison, Blakeman, Taylor & Co., New York: 38.
8. Darwin C (1888) *The Movements And Habits Of Climbing Plants*. Appleton, New York IV: 55.
9. McMillen T, Goriely A (2002) Tendril perversion in intrinsically curved rods. *J Nonlinear Sci* 12: 241–281.
10. Gerbode SJ, Puzey JR, McCormick AG, Mahadevan L (2012) How the cucumber tendril coils and overwinds. *Science* 337: 1087–1090.
11. Listing JB (1847) *Vorstudien über topologie*, I. *Göttinger Studien* : 811–875.
12. Maxwell MC (1873) *A treatise on electricity and magnetism*, II. Clarendon, Oxford : 456.
13. Goriely A, Tabor M (1998) Spontaneous helix hand reversal and tendril perversion in climbing plants. *Phys Rev Lett* 80: 1564–1567.
14. Chapman RE (1965) The ovine arrector pili musculature and crimp formation in wool. In *Biology of the Skin and Hair Growth* Angus and Robertson: Sydney.
15. Huang J, Liu J, Benedikt K, Bertoldi K, Clarke DR (2012) Spontaneous and deterministic three-dimensional curling of pre-strained elastomeric bi-strips. *Soft Matter* 8: 6291–6300.
16. Savin T, Kurpios NA, Shyer AE, Florescu P, Liang H, et al. (2011) On the growth and form of the gut. *Nature* 476: 57–62.
17. Sharon E, Roman B, Marder M, Shin GS, Swinney HL (2002) Buckling cascades in free sheets. *Nature* 419: 579.
18. Sharon E, Marder M, Swinney H (2004) Leaves, owers and garbage bags: making waves. *Am Sci* 92: 254–261.
19. Sharon E, Roman B, Swinney HL (2007) Geometrically driven wrinkling observed in free plastic sheets and leaves. *Phys Rev E* 75: 046211-1–046211-7.
20. Audoly B, Boudaoud A (2002) Ruban a godets: an elastic model for ripples in plant leaves. *C R Mecanique* 330: 831–836.
21. Marder M, Sharon E, Smith S, Roman B (2003) Theory of edges of leaves. *Europhys Lett* 62(4): 498–504.
22. Gent AN (1996) A new constitutive relation for rubber. *Rubber Chem Technol* 69: 59–61.
23. Kirchhoff G (1859) Über das Gleichgewicht und die Bewegung eines unendlich dfinnen elastischen Stabes. *J f reine, angew Math* 56: 285–313.
24. Kirchhoff G (1876) *Vorlesungen fiber mathematische Physik*. *Mechanik* 28.
25. Audoly B, Pomeau Y (2010) *Elasticity and geometry*. *Oxford University Press*.
26. Bower AF (2009) *Applied mechanics of solids*. *CRC Press. Taylor and Francis Group*.
27. Coleman BD, Dill EH, Lembo M, Lu Z, Tobias I (1993) On the dynamics of rods in the theory of Kirchhoff and Clebsch. *Arch Rational Mech Anal* 121: 339–359.
28. Young W, Budynas R (2002) *Roark's formulas for stress & strain*, 7th Edition.
29. Goriely A, Tabor M (1997) Nonlinear dynamics of filaments I. Dynamical instabilities. *Physica D* 105: 20–44.
30. Goriely A, Tabor M (1997) Nonlinear dynamics of filaments II. Nonlinear analysis. *Physica D* 105: 45–61.
31. Goriely A (2000) The nonlinear dynamics of filaments. *Nonlinear Dynam* 21: 101–133.
32. Goriely A, Shipman P (2000) Dynamics of helical strips. *Phys Rev E* 61: 4508–4517.
33. Balluffi RW, Allen SM, Carter WC (2005) *Kinetics of materials*. *Wiley Interscience*.
34. Patricio P, Adda-Bedia M, Amar MB (1998) An elastica problem: instability of an elastic arch. *Physica D* 124: 285–295.
35. Zhou H, Ou-Yang Z (1999) Spontaneous curvature-induced dynamical instability of Kirchhoff filaments: Application to DNA kink deformations. *J Chem Phys* 110: 1247–1251.
36. Valverde J, Van der Heijden GHM (2010) Magnetically-induced buckling of a whirling conducting rod with applications to electrodynamic space tethers. *J Nonlinear Sci* 20: 309–339.

Supplementary Material for the article
”From helices to hemihelices”

Jia Liu^{+,1}, Jiangshui Huang^{+,1}, Tianxiang Su⁺, Katia Bertoldi^{+,*,2}, and David R.
Clarke^{+,2}

⁺*School of Engineering and Applied Sciences, Harvard University, Cambridge, MA 02138*

^{*}*Kavli Institute, Harvard University, Cambridge, MA 02138*

¹*Contributed equally to this work*

²*To whom correspondence may be addressed. E-mail: bertoldi@seas.harvard.edu and
clarke@seas.harvard.edu*

We present three sets of supplemental materials:

- S1** Description of the experimental arrangement and sequences of images captured from video recordings of the unloading of stretched bi-strips. Details are given in the figure captions.
- S2** Details of the finite element simulations used to produce the simulation results presented in the text.
- S3** Full details of the Kirchhoff analysis as well as the stability and instability to perturbations that leads to the analytical findings presented in the text.

S1 Experimental loading arrangement, video sequences and phase diagram obtained under non-rotating end conditions

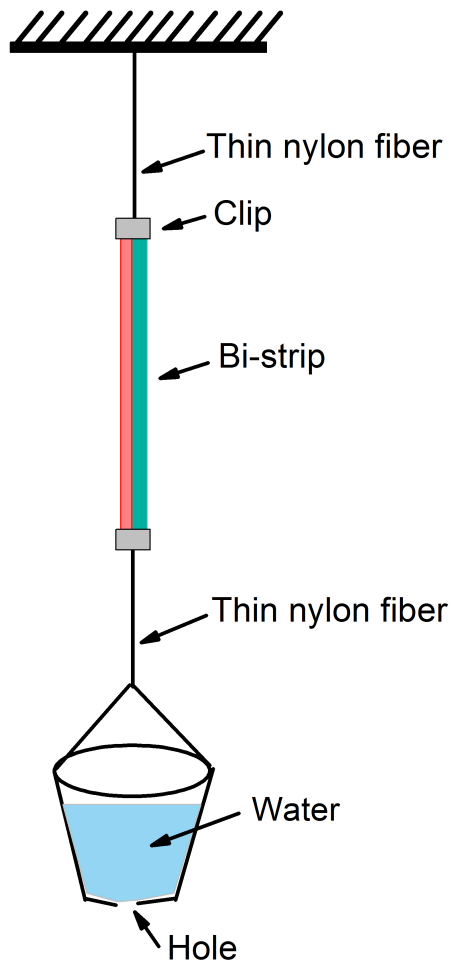


Figure S1: Experimental configuration used to alter the force stretching the bi-strip while allowing both ends of the bi-strip to freely rotate. The gravitational force on the weight attached to the bottom of the bi-strip stretches it. The weight consists of a container filled with either water or ball bearings. As the water or metal balls flow out of the container, the gravitational force applied to the bi-strip through the nylon fiber gradually decreases. The same configuration, with metal balls, was used to perform some experiments in water rather than in air to dampen transients.

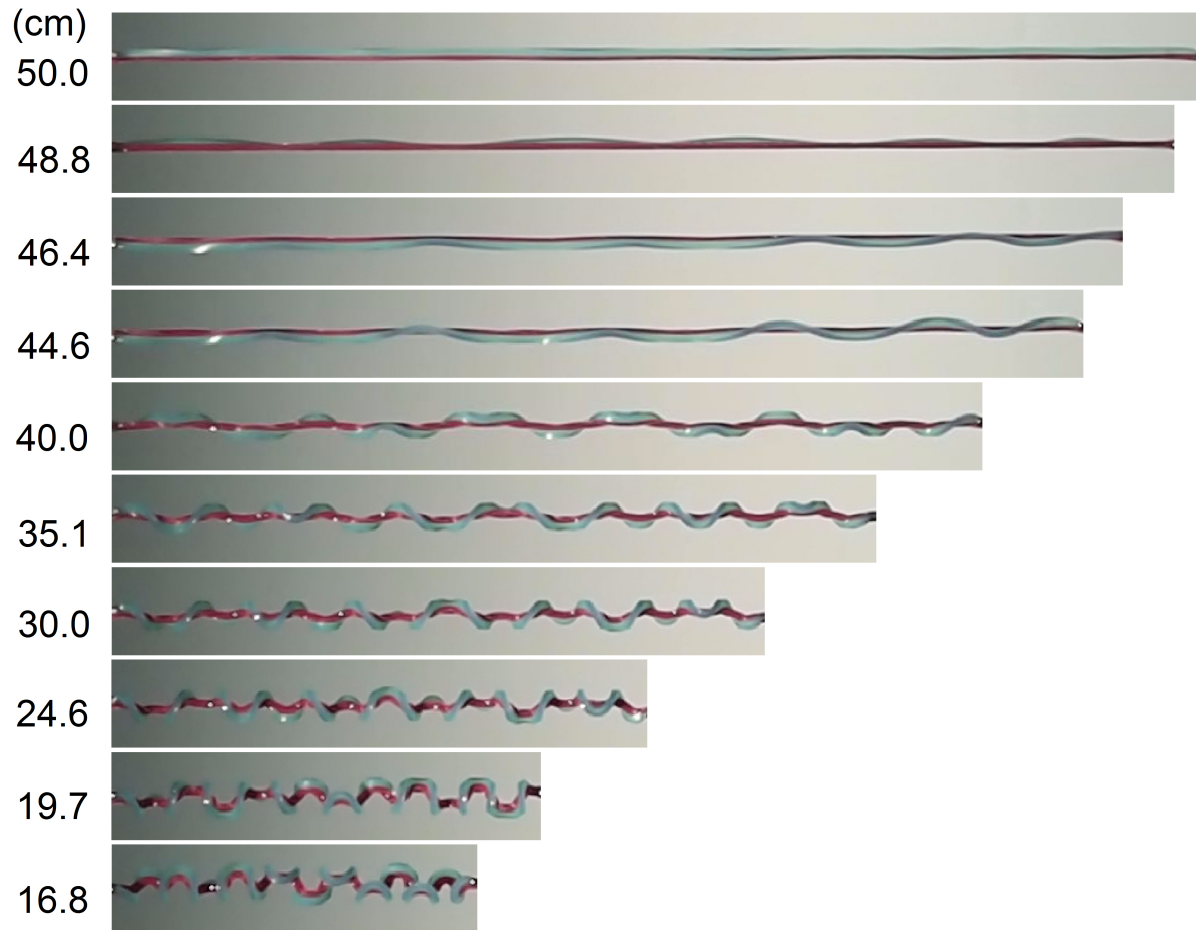


Figure S2: Sequence of images as the stretching force applied to the ends of a bi-strip is slowly reduced showing the formation of a hemihelix with eleven perversions. Width $w=3\text{mm}$, thickness $h=2.5\text{mm}$, length $L=50\text{ cm}$, and $\chi=1.5$ (Video S1). The distance between the two ends of the bi-strip indicated at the side of each image, decreases as the force is decreased. Perversions appear to form immediately unloading commences and while their amplitude steadily increases, their number remains unchanged.

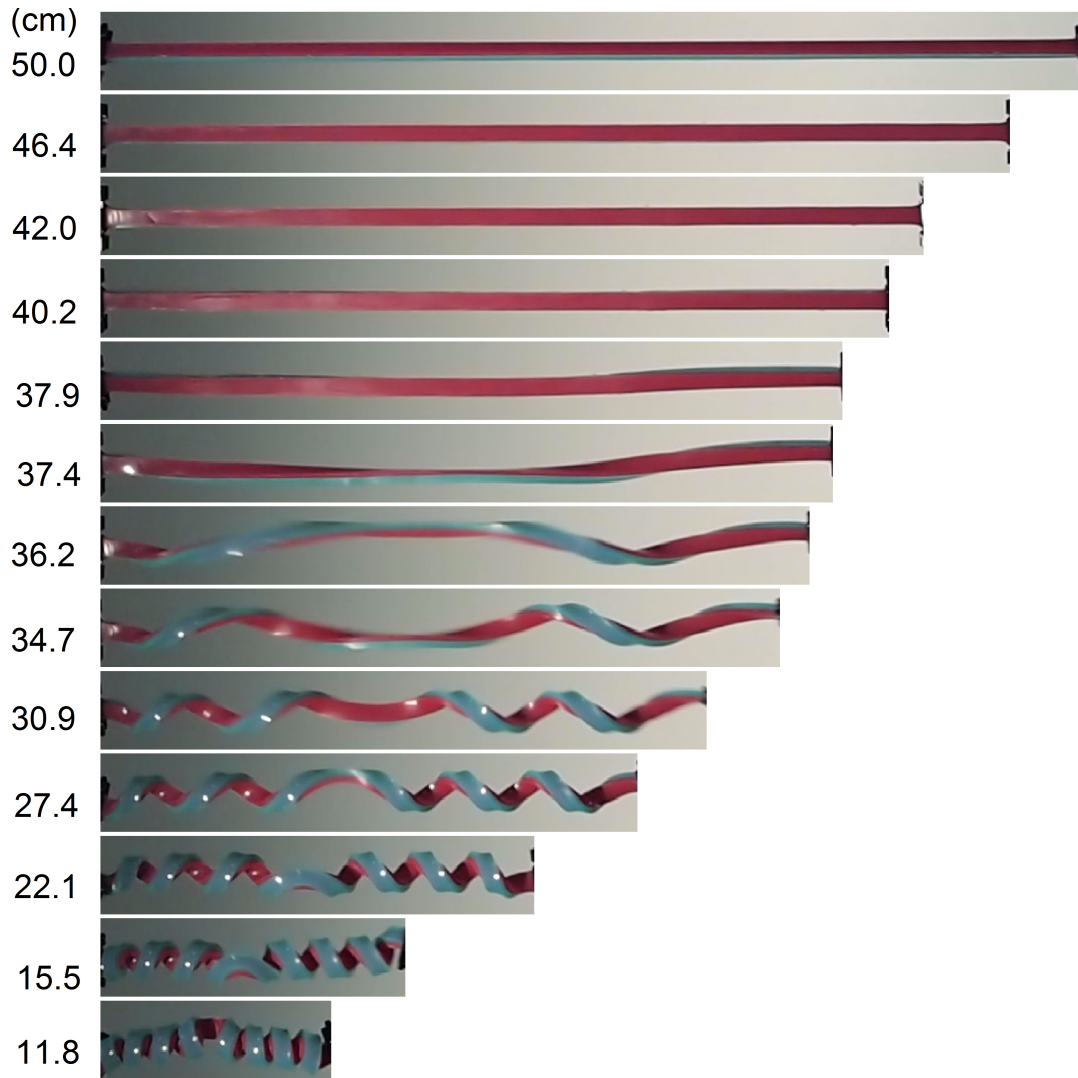


Figure S3: Similar images to those in figure S2 for a bi-strip of the same dimensions except that the thickness is $h=8\text{mm}$ (Video S2). As the distance between the two ends decreases, the bi-strip initially remains straight and flat but then a single perversion begins to form in the middle and grows to separate two helices of opposite chirality.

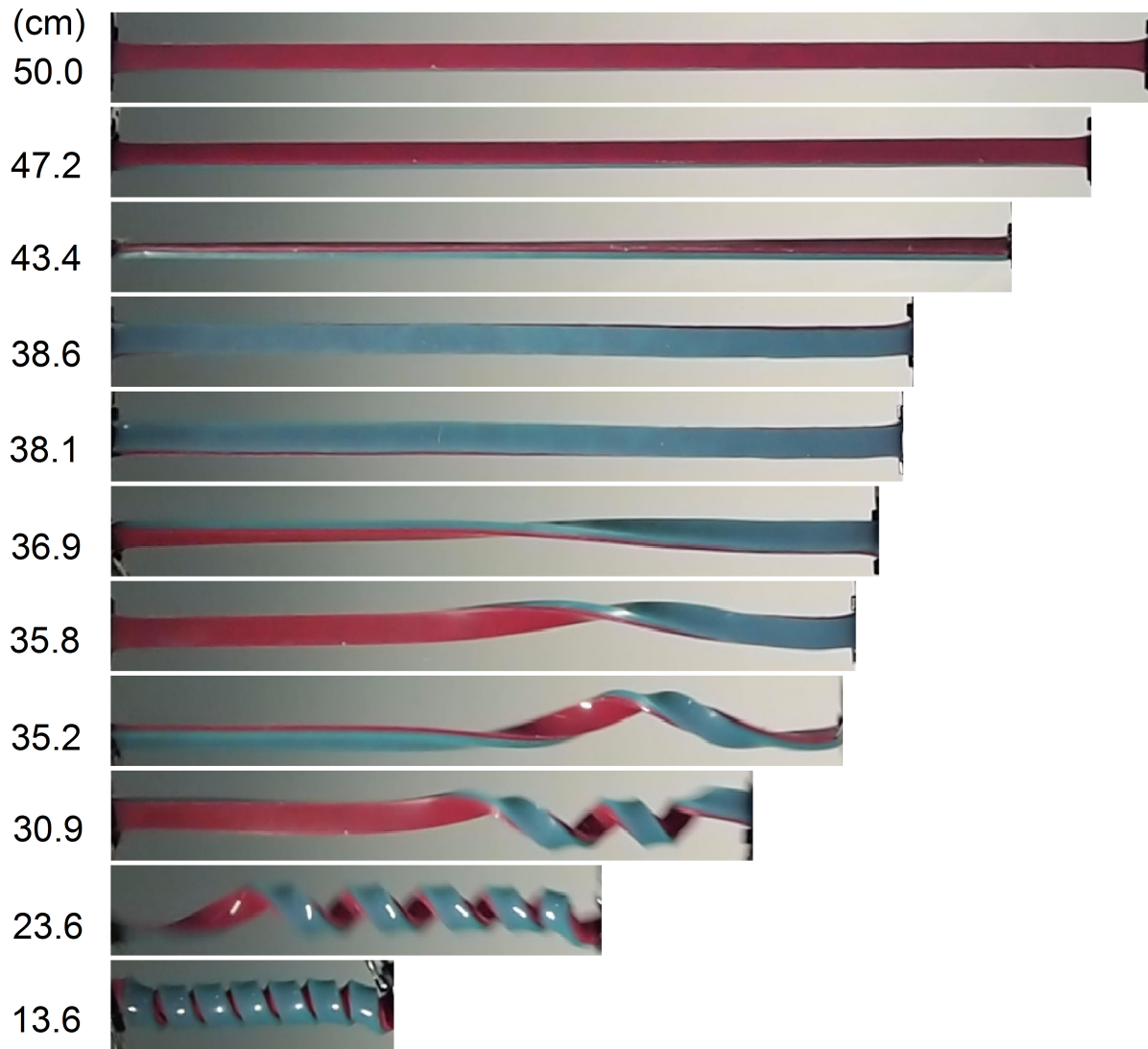


Figure S4: A sequence of images illustrating the formation of a simple helix upon unloading. (Video S3). Images of the unloading of a similar strip as in figure S2 and S3 except the strip had a greater thickness, $h = 12$ mm. At first, although the bi-strip rotates about its long axis, it remains straight and flat. As the distance is decreased further, an initial twist develops near the right-hand end, grows and then propagates along the bi-strip to form a simple helix.

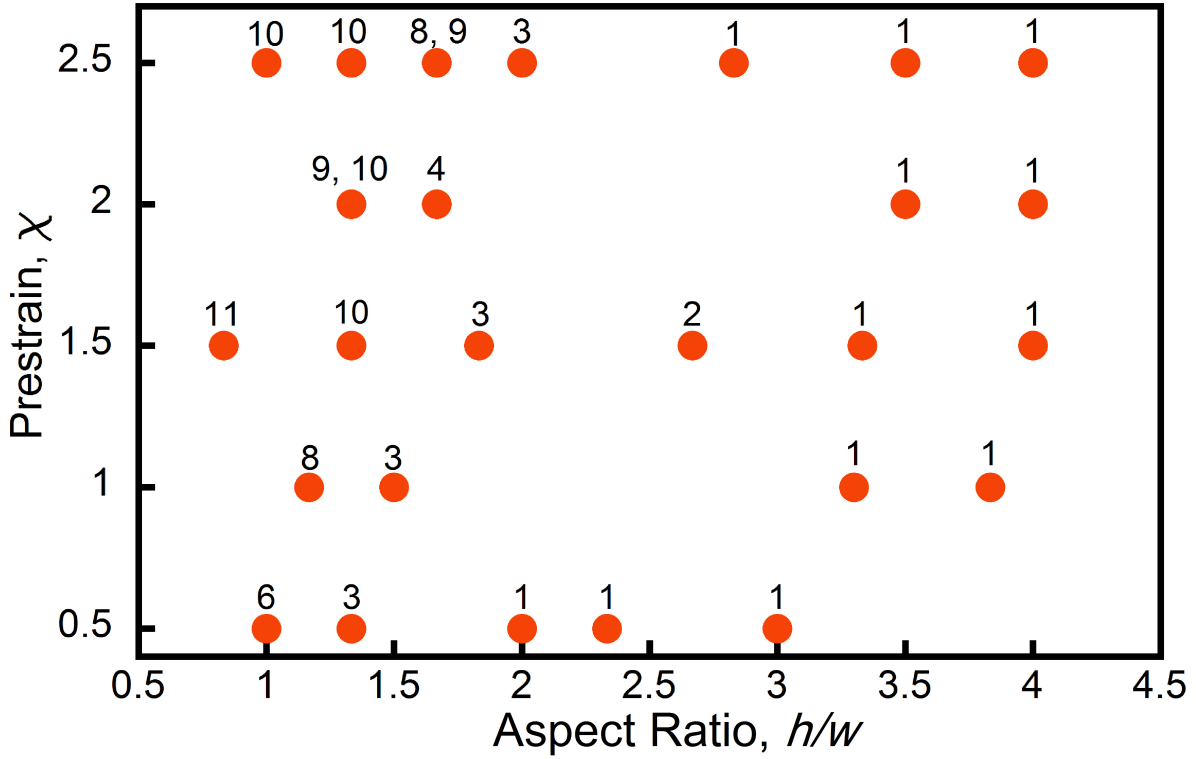


Figure S5: Phase diagram obtained when both ends of the bi-strip are clamped to prevent them from rotating. Compared to the phase diagram when the ends are free to rotate, the main difference is that helices do not form. Also, the number of perversions formed can be slightly different. For example, for $h/w = 2.67$ and $\chi = 1.5$, there is only one perversion when the ends can rotate but two perversions when they are clamped. The length, L , is 50 cm for each bi-strip.

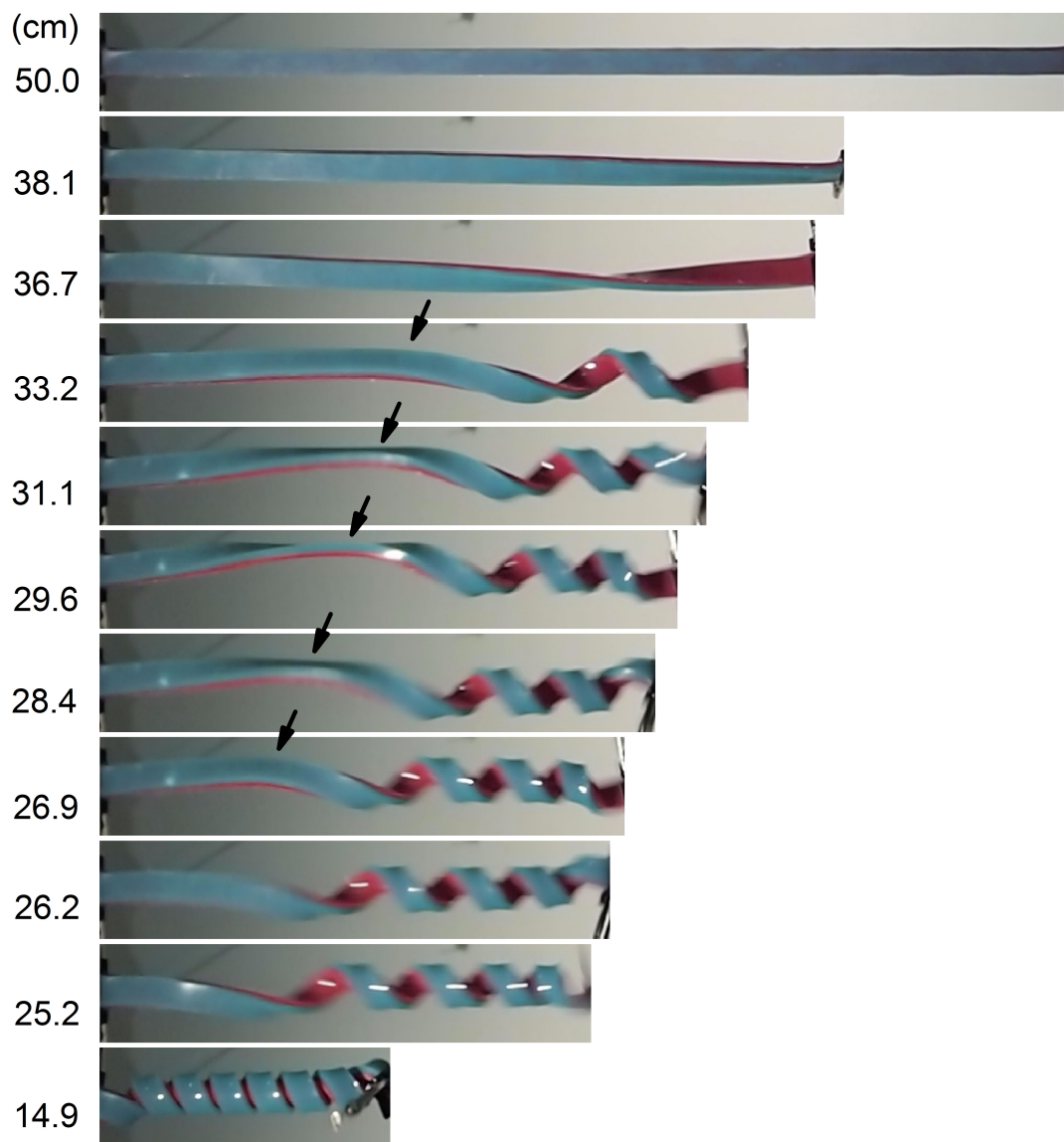


Figure S6: Images of the unloading of the same strip as in figure S4, but under a fixed boundary condition at the left end and free to rotate at the right end end (Video S7). In the process of forming a helix, a single perversion, marked by the arrow, begins to form but is then eliminated.

S2 Finite Element Simulations

To study the formation of the helices and hemi-helices and the conditions under which they form, the combination of twisting, compression and bending, together with the highly nonlinear constitutive behavior of elastomer need to be included. To simulate this complicated behavior, we first use finite element numerical simulations. Before describing these simulations in detail, the constitutive behavior of the elastomer is presented.

S2.1 The material model

Uniaxial tensile stress-strain tests performed on the bulk material show that it exhibits a large strain elastic behavior typical of elastomers with significant stiffening [1]. To capture the observed deformation response we modeled the material as a hyper-elastic solid and computed the stresses and elastic energies using the nearly-incompressible Gent model [10]. Here we briefly review the mathematical description of the model as well as basic concepts in the theory of large deformation.

Formally, we denote \mathbf{X} as the position vector of a material point in the undeformed configuration. During deformation, the material point gains a new position, which is marked by \mathbf{x} . The mapping matrix $\mathbf{F} = \partial\mathbf{x}/\partial\mathbf{X}$, named the deformation gradient, therefore connects the undeformed and deformed states. The determinant of the matrix $J = \det(\mathbf{F})$ represents the local volume change of the bulk material. For an isotropic hyperelastic material, the strain energy density W , is a function of the invariants of the left Cauchy-Green tensor $\mathbf{B} = \mathbf{F}\mathbf{F}^T$:

$$W = W(I_1, I_2, I_3), \quad (\text{S1})$$

where

$$I_1 = \text{tr}(\mathbf{B}), \quad I_2 = [(\text{tr}\mathbf{B})^2 - \text{tr}\mathbf{B}^2], \quad I_3 = \det(\mathbf{B}) = J^2. \quad (\text{S2})$$

Consequently, the Cauchy stress, a measure of the force acting on an element of area in the deformed material, is given by:

$$\boldsymbol{\sigma} = \frac{2}{J} \frac{\partial W}{\partial I_1} \mathbf{B} + \frac{\partial W}{\partial J} \mathbf{I}, \quad (\text{S3})$$

where \mathbf{I} is the identity tensor.

Particularly, for the Gent model, the strain energy density is,

$$W = -\frac{\mu}{2} J_m \ln \left(1 - \frac{I_1 - 3}{J_m} \right) - \mu \ln J + \left(\frac{K}{2} - \frac{\mu}{J_m} \right) (J - 1)^2, \quad (\text{S4})$$

where μ and K are the initial shear and bulk moduli, respectively, and J_m is a parameter related with the strain saturation. Eqn. (S3) then suggests the Cauchy stress is:

$$\boldsymbol{\sigma} = \frac{\mu J_m}{J(J_m - I_1 + 3)} \mathbf{B} - \frac{\mu}{J} \mathbf{I} + \left(K - \frac{2\mu}{J_m} \right) (J - 1) \mathbf{I}. \quad (\text{S5})$$

Additionally, we can obtain the nominal stress $\mathbf{s} = J\boldsymbol{\sigma} \cdot \mathbf{F}^{-T}$, which measures the force acting on an element of area in the undeformed configuration,

$$\mathbf{s} = \frac{\mu J_m}{J_m - I_1 + 3} \mathbf{F} - \mu \mathbf{F}^{-T} + \left(K - \frac{2\mu}{J_m} \right) J(J - 1) \mathbf{F}^{-T}. \quad (\text{S6})$$

The parameters μ , K , and J_m are obtained by fitting to the experimental tensile load-displacement curves, yielding values $\mu = 0.06\text{MPa}$, $K = 24\text{MPa}$ and $J_m = 28.2$ [1].

To account for the prestrain ratio χ , we decompose the deformation gradient into a load-induced part \mathbf{F}^L and a prestretch induced part \mathbf{F}^S following the multiplicative decomposition method originally introduced by Kroner and Lee [11, 12],

$$\mathbf{F} = \mathbf{F}^L \mathbf{F}^S, \text{ with } \mathbf{F}^S = \text{diag}(\chi + 1, 1/\sqrt{\chi + 1}, 1/\sqrt{\chi + 1}). \quad (\text{S7})$$

S2.2 Numerical Analysis

The commercial FE software Abaqus FEA was used for the analysis, employing the the Abaqus/Explicit solver. The material model was implemented into Abaqus/Explicit through user defined subroutine VUMAT. Three-dimensional models are built using 3D linear reduced integration elements (ABAQUS element type C3D8R). The accuracy of each mesh was ascertained through a mesh refinement study. Thereafter, dynamic explicit simulations were performed and quasi-static conditions were ensured by monitoring the kinetic energy and introducing a small damping factor. The analyses were performed under force control.

S3 Analytical Model

S3.1 The Kirchhoff model

The Kirchhoff model provides a well-established framework to study the statics and dynamics of elastic rods [13, 14]. In this section we introduce the basic notations, briefly review the derivation of the Kirchhoff equations and finally summarize how the stability of a rod can be investigated by studying perturbed states of the system.

S3.1.1 Kinematics

We consider an inextensible and unshearable rod in the 3D space [3, 7, 8], whose centerline is described by a position vector $\mathbf{x}(s, t)$, where s is the arc-length and t is the time (see Fig. S7). Note that due to the inextensible assumption, the total length L of the rod does not change during deformation, so that $s \in [0, L]$. In addition, a local director basis

$$(\mathbf{d}_1, \mathbf{d}_2, \mathbf{d}_3) = (\mathbf{d}_1(s, t), \mathbf{d}_2(s, t), \mathbf{d}_3(s, t)), \quad (\text{S8})$$

is associated to the rod and the vector \mathbf{d}_3 is identified as the unit tangent vector to the curve,

$$\mathbf{d}_3 \equiv \mathbf{x}', \quad (\text{S9})$$

where here and in what follows $(\cdot)' = \partial(\cdot)/\partial s$. Furthermore, \mathbf{d}_1 and \mathbf{d}_2 are two unit vectors in the plane normal to \mathbf{d}_3 , so that $(\mathbf{d}_1, \mathbf{d}_2, \mathbf{d}_3)$ forms a right-handed triad (i.e. $\mathbf{d}_2 = \mathbf{d}_3 \times \mathbf{d}_1$, $\mathbf{d}_1 = \mathbf{d}_2 \times \mathbf{d}_3$). For the sake of simplicity, \mathbf{d}_1 and \mathbf{d}_2 are chosen to lie along the principal axes of inertia of the cross-section.

The condition of orthonormality implies the existence of a twist vector $\boldsymbol{\kappa} = \kappa_1 \mathbf{d}_1 + \kappa_2 \mathbf{d}_2 + \kappa_3 \mathbf{d}_3$ satisfying

$$\mathbf{d}'_i = \boldsymbol{\kappa} \times \mathbf{d}_i, \quad i = 1, 2, 3, \quad (\text{S10})$$

so that

$$\mathbf{d}'_1 = -\kappa_2 \mathbf{d}_3 + \kappa_3 \mathbf{d}_2, \quad \mathbf{d}'_2 = \kappa_1 \mathbf{d}_3 - \kappa_3 \mathbf{d}_1, \quad \mathbf{d}'_3 = -\kappa_1 \mathbf{d}_2 + \kappa_2 \mathbf{d}_1. \quad (\text{S11})$$

κ_1 and κ_2 are called material curvatures and express how much the frame $(\mathbf{d}_1, \mathbf{d}_2, \mathbf{d}_3)$ rotates about the directions \mathbf{d}_1 and \mathbf{d}_2 of the cross section. In contrast, κ_3 is called the twist density and expresses how much the director frame rotates about the direction \mathbf{d}_3 .

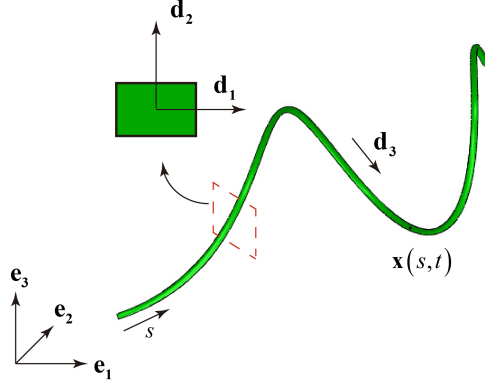


Figure S7: The configuration of an elastic rod is represented by a curve $\mathbf{x}(s, t)$ and by a local director basis $(\mathbf{d}_1, \mathbf{d}_2, \mathbf{d}_3)$.

S3.1.2 Dynamics

In Kirchhoff's theory of elastic rods all physically relevant stresses are considered as cross-sectional averages at each point along the axis of the rod. Kirchhoff equations relate the resultant force \mathbf{F} and moment \mathbf{M} acting on the cross section to the director basis.

Let $\mathbf{p} = \mathbf{p}(s, X_1, X_2, t)$ be the Piola stress vector, where X_1 and X_2 are the coordinates along the principal directions on the cross-section. The Piola stress vector \mathbf{p} gives the density of the elastic forces exerted on the material surface $\Omega(s)$ by the material on the side of increasing s at the point with material coordinates (s, X_1, X_2) . The resultant force acting on the cross section $\Omega(s)$ is then given by

$$\mathbf{F} = \mathbf{F}(s, t) = \iint_{\Omega(s)} \mathbf{p} dX_1 dX_2. \quad (\text{S12})$$

Similarly, the resultant moment about $\mathbf{x}(s, t)$ of the stresses acting on $\Omega(s)$ is

$$\mathbf{M} = \mathbf{M}(s, t) = \iint_{\Omega(s)} \mathbf{r} \times \mathbf{p} dX_1 dX_2, \quad (\text{S13})$$

where the vector \mathbf{r} is defined so that

$$\mathbf{y}(s, X_1, X_2, t) = \mathbf{x}(s, t) + \mathbf{r}(s, X_1, X_2, t), \quad (\text{S14})$$

with \mathbf{y} denoting the position vector of an arbitrary material point on the cross-section.

When no external forces/moments are applied, the balance laws for linear and angular momentum yield

$$\begin{aligned} \frac{d\mathbf{F}}{ds} &= \iint_{\Omega(s)} \rho \dot{\mathbf{y}} dX_1 dX_2, \\ \frac{d\mathbf{M}}{ds} + \frac{d\mathbf{x}}{ds} \times \mathbf{F} &= \iint_{\Omega(s)} \rho \mathbf{r} \times \dot{\mathbf{y}} dX_1 dX_2, \end{aligned} \quad (\text{S15})$$

where $(\dot{\cdot}) = \partial(\cdot)/\partial t$ and ρ is the density (mass per unit volume) that is taken to be constant during deformation. Since for an unshearable rod (i.e. a rod for whose cross-section only undergoes rigid body motion during deformation) the position of a material point \mathbf{y} on the cross-section is given by

$$\mathbf{y}(s, X_1, X_2, t) = \mathbf{x}(s, t) + \mathbf{r}(s, X_1, X_2, t) = \mathbf{x}(s, t) + X_1 \mathbf{d}_1(s, t) + X_2 \mathbf{d}_2(s, t), \quad (\text{S16})$$

Eqns. (S15) become

$$\mathbf{F}' = \rho A \ddot{\mathbf{x}}, \quad (\text{S17})$$

$$\mathbf{M}' + \mathbf{d}_3 \times \mathbf{F} = \rho \left(I_2 \mathbf{d}_1 \times \ddot{\mathbf{d}}_1 + I_1 \mathbf{d}_2 \times \ddot{\mathbf{d}}_2 \right), \quad (\text{S18})$$

where A is the cross-sectional area and I_1 and I_2 are the principal moments of inertial of the cross section. Note that after differentiation with respect to s and use of Eqn. (S9), Eqn. (S17) can be rewritten as

$$\mathbf{F}'' = \rho A \ddot{\mathbf{d}}_3. \quad (\text{S19})$$

The Kirchhoff equations are then completed by the linear constitutive relation

$$\mathbf{M} = E I_1 (\kappa_1 - \kappa_1^{(u)}) \mathbf{d}_1 + E I_2 (\kappa_2 - \kappa_2^{(u)}) \mathbf{d}_2 + G J (\kappa_3 - \kappa_3^{(u)}) \mathbf{d}_3, \quad (\text{S20})$$

where J is the torsion constant which depends on the cross sectional shape, E and G are the Young's and shear modulus of the material, respectively. Moreover, in Eqn. (S20) we have introduced the intrinsic curvature $\boldsymbol{\kappa}^{(u)} = \kappa_1^{(u)} \mathbf{d}_1 + \kappa_2^{(u)} \mathbf{d}_2 + \kappa_3^{(u)} \mathbf{d}_3$ to describe a rod which in its unstressed state has a locally non-vanishing curvature. Finally, we note that the torsion constant J is defined as

$$J = \iint_{\Omega(s)} \left(X_1^2 + X_2^2 + X_1 \frac{\partial \Phi}{\partial X_2} - X_2 \frac{\partial \Phi}{\partial X_1} \right) dX_1 dX_2, \quad (\text{S21})$$

where Φ is the warping function for torsion given by the linear theory of elasticity. It has been shown that for a rectangular cross-section, J can be well approximated by [4]

$$J \approx ab^3 \left(\frac{1}{3} - 0.21 \frac{b}{a} \left(1 - \frac{b^4}{12a^4} \right) \right), \quad (\text{S22})$$

where a and b denote the length of the long and short side of the rectangular, respectively.

S3.1.3 Statics

If the system is in static equilibrium, the right-hand sides of eqns. (S17)–(S18) are zero, so that

$$\mathbf{F}' = 0, \quad (\text{S23})$$

$$\mathbf{M}' + \mathbf{d}_3 \times \mathbf{F} = 0.$$

Writing the resultant force as $\mathbf{F} = F_1 \mathbf{d}_1 + F_2 \mathbf{d}_2 + F_3 \mathbf{d}_3$ and projecting Eqns. (S23) along the director basis we obtain:

$$F_1' - F_2 \kappa_3 + F_3 \kappa_2 = 0, \quad (\text{S24})$$

$$F_2' - F_3 \kappa_1 + F_1 \kappa_3 = 0,$$

$$F_3' - F_1 \kappa_2 + F_2 \kappa_1 = 0,$$

$$E I_1 \kappa_1' - E I_2 (\kappa_2 - \kappa_2^{(u)}) \kappa_3 + G J (\kappa_3 - \kappa_3^{(u)}) \kappa_2 - F_2 = 0,$$

$$E I_2 \kappa_2' - G J (\kappa_3 - \kappa_3^{(u)}) \kappa_1 + E I_1 (\kappa_1 - \kappa_1^{(u)}) \kappa_3 + F_1 = 0,$$

$$G J \kappa_3' - E I_1 (\kappa_1 - \kappa_1^{(u)}) \kappa_2 + E I_2 (\kappa_2 - \kappa_2^{(u)}) \kappa_1 = 0.$$

S3.1.4 Stability

If the exact solution of the Kirchhoff equations is known, the stability of the configuration can be investigated by studying perturbed states of the systems in a small neighborhood of the reference solution [5, 6]. This can be systematically done by expanding the relevant variables \mathbf{d}_i and F_i as power series in a small parameter ϵ , which characterizes the distance from the reference configuration,

$$\mathbf{d}_i = \mathbf{d}_i^{(0)} + \epsilon \mathbf{d}_i^{(1)} + \epsilon^2 \mathbf{d}_i^{(2)} + \dots \quad i = 1, 2, 3, \quad (\text{S25})$$

$$F_i = F_i^{(0)} + \epsilon F_i^{(1)} + \epsilon^2 F_i^{(2)} + \dots \quad i = 1, 2, 3, \quad (\text{S26})$$

where $\mathbf{d}_i^{(0)}$ and $F_i^{(0)}$ denote the reference (unperturbed) director basis and force components, respectively. Since the orthonormality condition requires $\mathbf{d}_i \cdot \mathbf{d}_j = \delta_{ij}$, the perturbed basis $\mathbf{d}_i^{(j)}$ can be expressed in terms of the unperturbed basis $\mathbf{d}_i^{(0)}$ as

$$\mathbf{d}_i^{(1)} = \sum_{j=1}^3 A_{ij}^{(1)} \mathbf{d}_j^{(0)}, \quad (\text{S27})$$

$$\mathbf{d}_i^{(2)} = \sum_{j=1}^3 (A_{ij}^{(2)} + S_{ij}^{(2)}) \mathbf{d}_j^{(0)}, \quad (\text{S28})$$

\vdots

$$\mathbf{d}_i^{(n)} = \sum_{j=1}^3 (A_{ij}^{(n)} + S_{ij}^{(n)}) \mathbf{d}_j^{(0)}, \quad (\text{S29})$$

where $\mathbf{A}^{(k)}$ is an antisymmetric matrix

$$\mathbf{A}^{(k)} = \begin{pmatrix} 0 & \alpha_3^{(k)} & -\alpha_2^{(k)} \\ -\alpha_3^{(k)} & 0 & \alpha_1^{(k)} \\ \alpha_2^{(k)} & -\alpha_1^{(k)} & 0 \end{pmatrix}. \quad (\text{S30})$$

Furthermore, $\mathbf{S}^{(k)}$ is a symmetric matrix whose entries are only a function of $\alpha_i^{(j)}$ with $j < k$. In particular, $\mathbf{S}^{(2)}$ can be obtained explicitly as

$$\mathbf{S}^{(2)} = \frac{1}{2} \begin{pmatrix} -(\alpha_2^{(1)})^2 - (\alpha_3^{(1)})^2 & \alpha_1^{(1)} \alpha_2^{(1)} & \alpha_1^{(1)} \alpha_3^{(1)} \\ \alpha_1^{(1)} \alpha_2^{(1)} & -(\alpha_3^{(1)})^2 - (\alpha_1^{(1)})^2 & \alpha_2^{(1)} \alpha_3^{(1)} \\ \alpha_1^{(1)} \alpha_3^{(1)} & \alpha_2^{(1)} \alpha_3^{(1)} & -(\alpha_1^{(1)})^2 - (\alpha_2^{(1)})^2 \end{pmatrix}. \quad (\text{S31})$$

We also notice that the components of the twist vector $\boldsymbol{\kappa} = \kappa_1 \mathbf{d}_1 + \kappa_2 \mathbf{d}_2 + \kappa_3 \mathbf{d}_3$ can be written in terms of the perturbed variables as [9]:

$$\mathbf{K} = \left(\mathbf{B} \mathbf{K}^{(0)} + \frac{\partial \mathbf{B}}{\partial s} \right) \mathbf{B}^{-1}, \quad (\text{S32})$$

where

$$\mathbf{K} = \begin{pmatrix} 0 & \kappa_3 & -\kappa_2 \\ -\kappa_3 & 0 & \kappa_1 \\ \kappa_2 & -\kappa_1 & 0 \end{pmatrix}, \quad \mathbf{K}^{(0)} = \begin{pmatrix} 0 & \kappa_3^{(0)} & -\kappa_2^{(0)} \\ -\kappa_3^{(0)} & 0 & \kappa_1^{(0)} \\ \kappa_2^{(0)} & -\kappa_1^{(0)} & 0 \end{pmatrix}, \quad (\text{S33})$$

and

$$\mathbf{B} = \mathbf{I} + \epsilon \mathbf{A}^{(1)} + \epsilon^2 \left(\mathbf{A}^{(2)} + \mathbf{S}^{(2)} \right) + \dots \quad (\text{S34})$$

Substituting (S25) and (S26) into the governing equations (S18) and (S19), and defining the stationary configuration in terms of the six-dimensional vector $\boldsymbol{\mu}^{(0)} = \left(\alpha_1^{(0)}, \alpha_2^{(0)}, \alpha_3^{(0)}, F_1^{(0)}, F_2^{(0)}, F_3^{(0)} \right)$, the Kirchhoff equations to order k are obtained as

$$O(\epsilon^0) : \mathbf{E}(\boldsymbol{\mu}^{(0)}) = \mathbf{0}, \quad (\text{S35})$$

$$O(\epsilon^1) : \mathbf{L}(\boldsymbol{\mu}^{(0)}) \cdot \boldsymbol{\mu}^{(1)} = \mathbf{0}, \quad (\text{S36})$$

$$O(\epsilon^2) : \mathbf{L}(\boldsymbol{\mu}^{(0)}) \cdot \boldsymbol{\mu}^{(2)} = \mathbf{H}_2(\boldsymbol{\mu}^{(1)}), \quad (\text{S37})$$

⋮

where $\boldsymbol{\mu}^{(k)} = \left(\alpha_1^{(k)}, \alpha_2^{(k)}, \alpha_3^{(k)}, F_1^{(k)}, F_2^{(k)}, F_3^{(k)} \right)$, $\mathbf{E}(\boldsymbol{\mu}^{(0)}) = \mathbf{0}$ describes the trivial static solution, $\mathbf{L}(\cdot)$ is a linear operator and $\mathbf{H}_2(\cdot)$ is a quadratic operator. It is worth noting that eqns. (S35), (S36) and (S37) have to be solved sequentially.

Finally, we note that when $\boldsymbol{\mu}^{(1)}$ and $\boldsymbol{\mu}^{(2)}$ are known, the solution $\mathbf{x} = \mathbf{x}^{(0)} + \epsilon \mathbf{x}^{(1)} + \epsilon^2 \mathbf{x}^{(2)}$ can be reconstructed as

$$\mathbf{x} = \int \mathbf{d}_3 ds = \int \left(\mathbf{d}_3^{(0)} + \epsilon \mathbf{d}_3^{(1)} + \epsilon^2 \mathbf{d}_3^{(2)} \right) ds. \quad (\text{S38})$$

In Section S3.2.3 we will show that all the 3D complex shapes observed during the release process in our experiments can be captured conducting the stability analysis outlined above.

S3.2 Modeling of pre-strained elastomeric bi-strips

This study focuses on the investigation of the complex shapes that can be produced by a simple generic process consisting of pre-straining one elastomeric strip, joining it side-by-side to another and then releasing the bi-strip. To predict such shapes analytically, the pre-strained elastomeric bi-strip is modeled as a rod with homogeneous rectangular cross section and intrinsic curvature, so that its response can be described by Kirchhoff equations. In this section we first describe how the intrinsic curvature of the equivalent rod can be obtained (Section S3.2.1), then investigate two simple equilibrium solutions to the Kirchhoff equations (Section S3.2.2) and finally study the stability of the rod (Section S3.2.3) and the mode selection process (Section S3.2.4) as the tension is slowly released.

S3.2.1 Intrinsic curvature of the equivalent rod

In the physical system considered in this study we have two strips: one non-prestretched and one prestretched. For the sake of clarity, in this section we use the subscripts a and b to denote quantities related to the non-prestretched and prestretched strips, respectively. Note that L_a , w_a and h_a correspond to L , w and h in the main text (which are the length, width and height, respectively), while L_b , w_b and h_b are denoted as L' , w' and h in the main document. The two strips are different in initial length so that $L_a \neq L_b$. When the shorter strip is stretched to the length of the longer one and bonded to it, it is expected that they together will curve along the bonding layer and form an arc with angle θ and curvature K , as shown in Fig. S8(a). Therefore, the bi-strip can be modeled as a rod with homogeneous cross-section, intrinsic curvature $(\kappa_1^{(u)}, \kappa_2^{(u)}, \kappa_3^{(u)}) = (K, 0, 0)$ and length $L_* = R\theta$ (see Fig. S8(b)), with R denoting the radius from the center of the arc to the interface of the two bonded strips. Now we determine

the curvature K and the length L_* as functions of the dimensions and material properties of the two strips.

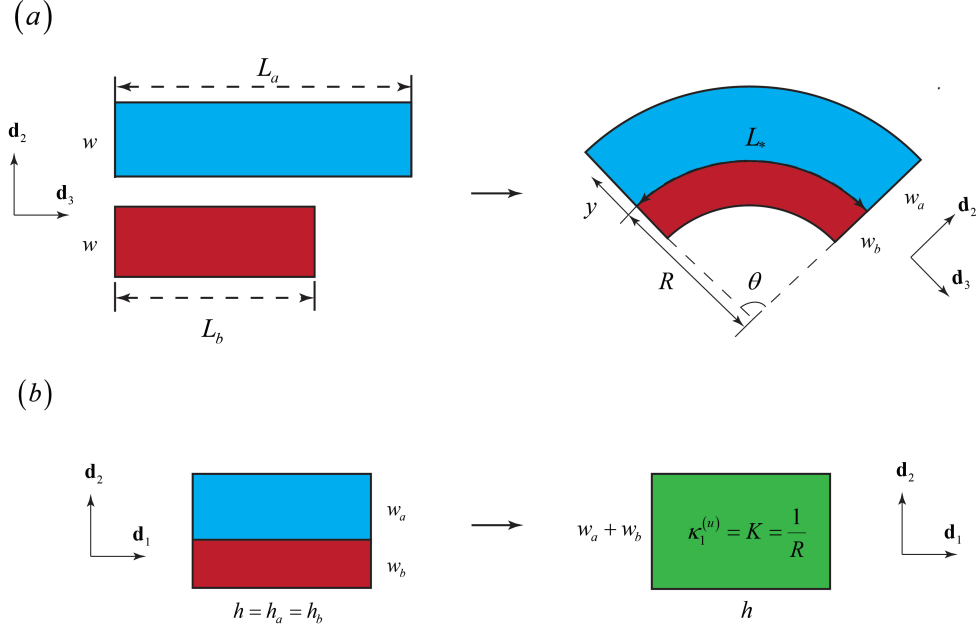


Figure S8: (a) The pre-straining operation used to form the bi-strip. Strip b is stretched until it has the same length as strip a . Then two strips are then glued together and curve along the bonding layer, forming an arc with angle θ , curvature K and length L_* . (b) The bi-strip is modeled as a rod with homogeneous cross-section, intrinsic curvature $(\kappa_1^{(u)}, \kappa_2^{(u)}, \kappa_3^{(u)}) = (K, 0, 0)$ and length $L_* = R\theta$.

Let y denote the width coordinate with $y = 0$ at the interface of the two bonded strips. According to the elastic beam theory and the assumption of pure bending, the longitudinal strain ϵ at an arbitrary point on the cross section of the two strips is given by

$$\epsilon = \begin{cases} \frac{(R+y)\theta - L_a}{L_a} = \frac{L_* + y\theta}{L_a} - 1, & y > 0 \text{ for strip } a, \\ \frac{(R+y)\theta - L_b}{L_b} = \frac{L_* + y\theta}{L_b} - 1, & y < 0 \text{ for strip } b. \end{cases} \quad (\text{S39})$$

This deformation will result in a uniaxial state of stress, where only the normal stress σ along the longitudinal direction is non-vanishing. Mechanical equilibrium requires that the net forces and moments are zero, yielding

$$\begin{aligned} \int \sigma dA &= \int_0^{w_a} \sigma_a h_a dy + \int_{-w_b}^0 \sigma_b h_b dy = 0, \\ \int \sigma y dA &= \int_0^{w_a} \sigma_a y h_a dy + \int_{-w_b}^0 \sigma_b y h_b dy = 0, \end{aligned} \quad (\text{S40})$$

which can be solved to obtain K and L_* . Finally, we note that since in our physical system

$h_a = h_b$, Eqns. (S40) simplify to

$$\begin{aligned} \int_0^{w_a} \sigma_a dy + \int_{-w_b}^0 \sigma_b dy &= 0, \\ \int_0^{w_a} \sigma_a y dy + \int_{-w_b}^0 \sigma_b y dy &= 0. \end{aligned} \quad (\text{S41})$$

Linear model. For a linear elastic material, the axial stress in the strips is given by

$$\sigma = \begin{cases} E \left(\frac{L_* + y\theta}{L_a} - 1 \right), & y > 0 \text{ for strip } a \\ E \left(\frac{L_* + y\theta}{L_b} - 1 \right), & y < 0 \text{ for strip } b \end{cases} \quad (\text{S42})$$

Substitution of Eqns. (S42) into the equilibrium equations (S41) yields

$$\begin{aligned} \int_0^{w_a} \left(\frac{L_* + y\theta}{L_a} - 1 \right) dy + \int_{-w_b}^0 \left(\frac{L_* + y\theta}{L_b} - 1 \right) dy &= 0, \\ \int_0^{w_a} \left(\frac{L_* + y\theta}{L_a} - 1 \right) y dy + \int_{-w_b}^0 \left(\frac{L_* + y\theta}{L_b} - 1 \right) y dy &= 0. \end{aligned} \quad (\text{S43})$$

For the sake of simplicity, here we neglect the effect of the prestrain on the width of the strips and assume $w_a = w_b = w$, so that Eqns. (S43) reduce to

$$\begin{aligned} L_* \left(\frac{2}{L_a} + \frac{2}{L_b} \right) + \theta \left(\frac{w}{L_a} - \frac{w}{L_b} \right) - 4 &= 0, \\ L_* \left(\frac{3}{L_a} - \frac{3}{L_b} \right) + \theta \left(\frac{2w}{L_a} + \frac{2w}{L_b} \right) &= 0, \end{aligned} \quad (\text{S44})$$

from which L_* , θ and K can be obtained as

$$\begin{aligned} L_* &= L_a \frac{8(2 + \chi)}{2 + 14\chi + (\chi + 1)^2}, \\ \theta &= \frac{L_a}{w} \frac{12\chi}{2 + 14\chi + (\chi + 1)^2}, \\ K &= \frac{1}{w} \frac{12\chi}{8(2 + \chi)}. \end{aligned} \quad (\text{S45})$$

where $\chi = L_a/L_b - 1$ denotes the pre-strain.

Non-linear model. Following Huang et al. [1], we assume a fully incompressible elastomer (i.e. $\det(\mathbf{F}) = 1$), so that the state of deformation in each strip is fully characterized by

$$\mathbf{F} = \text{diag}(\lambda, 1/\sqrt{\lambda}, 1/\sqrt{\lambda}), \quad (\text{S46})$$

where \mathbf{F} is the deformation gradient and λ is the stretch

$$\lambda = \epsilon + 1 = \begin{cases} \frac{\theta(R + y)}{L_a} = \frac{L_* + y\theta}{L_a}, & y > 0 \text{ for strip } a, \\ \frac{\theta(R + y)}{L_b} = \frac{L_* + y\theta}{L_b}, & y < 0 \text{ for strip } b. \end{cases} \quad (\text{S47})$$

To capture the response of the elastomeric strips, we use the incompressible Gent model [10], so that the uniaxial stress is given by

$$\sigma = \left(\lambda^2 - \frac{1}{\lambda} \right) \frac{\mu J_m}{J_m - I_1 + 3}, \quad (\text{S48})$$

where $\mu = E/3$ is the initial shear modulus, J_m is a constant related to the strain saturation of the material and $I_1 = \lambda^2 + 2/\lambda$. Moreover, the width of each strip entering the evaluation of the integrals in Eqns. (S40) is calculated using the longitudinal stretch at the mid-plane in the current state,

$$w_a = \frac{w}{\sqrt{\lambda_a(y = w_a/2)}}, \quad w_b = \frac{w}{\sqrt{\lambda_b(y = -w_b/2)}}. \quad (\text{S49})$$

Unlike the linear model, Eqns. (S40), (S48) and (S49) cannot be solved analytically, so the trust-region-dogleg algorithm within Matlab software is used to solve numerically for K and L_* .

Results. We consider a bi-strip characterized by $w = 3 \text{ mm}$ and $L_a = 500 \text{ mm}$. In Fig. S9 we report the evolution of K and L_* as a function of the pre-strain χ for both the linear and non-linear model. The results show a good agreement between the two models. Therefore, for the sake of simplicity the linear model will be used in the stability analysis described in the following sections.

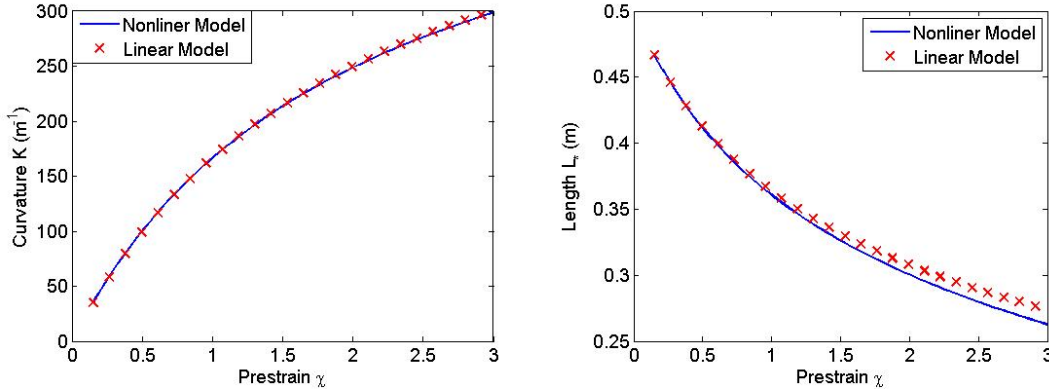


Figure S9: The curvature K and the length L_* as a function of the prestrain ($\chi = L_a/L_b - 1$) for a bi-strip with $h=3 \text{ mm}$, $w=3 \text{ mm}$, $L_a = 500 \text{ mm}$. The continuous blue line and the red markers correspond to the predictions from the linear and non-linear model, respectively.

S3.2.2 Equilibrium configurations of the equivalent rod

We now seek solutions of the static equilibrium equations (S24) for the equivalent rod with homogeneous rectangular cross section with edges $2w$ and h , length L_* and intrinsic curvature K given by (S45). Our starting point is the fully stretched state obtained by applying the tensile force P . Here, we first show that both the straight and helical configurations are equilibrium configurations for the system and then demonstrate that for large values of applied tension P the straight configuration is energetically favorable, while below a critical tensile force P_{cr} , the helical configuration grows.

Straight configuration A straight configuration (without twist) is characterized by,

$$\mathbf{d}_1 = \mathbf{e}_1, \mathbf{d}_2 = \mathbf{e}_2, \mathbf{d}_3 = \mathbf{e}_3, \quad (\text{S50})$$

so that

$$\kappa_1 = \kappa_2 = \kappa_3 = 0, \quad (\text{S51})$$

where \mathbf{e}_i is the basis director of the global coordinate system. Substitution of Eqns. (S50) and (S51) into the static equilibrium equations (S24) yields

$$F'_3 = 0, \quad F_1 = F_2 = 0. \quad (\text{S52})$$

Therefore, the rod is subjected to a uniform internal force $\mathbf{F} = P \mathbf{d}_3$, where P represents the loading parameter during the releasing process. Moreover, the constitutive relation (S20) implies that

$$\mathbf{M} = -E I_1 K \mathbf{d}_1. \quad (\text{S53})$$

Conclusively, a straight rod with internal force $\mathbf{F} = P \mathbf{d}_3$ and moment $\mathbf{M} = -E I_1 K \mathbf{d}_1$ is an equilibrium state. As a result, the energy density (total energy per length) of the straight configuration is given by

$$\mathcal{E} = \frac{1}{2} E I_1 K^2 - P. \quad (\text{S54})$$

Helical configuration An helical configuration with curvature κ and torsion τ is defined by the position vector

$$\mathbf{x} = \frac{\kappa}{\gamma^2} \sin(\gamma s) \mathbf{e}_1 + \frac{\kappa}{\gamma^2} (\cos(\gamma s) - 1) \mathbf{e}_2 + \frac{\tau}{\gamma} s \mathbf{e}_3, \quad (\text{S55})$$

where $\gamma = \sqrt{\tau^2 + \kappa^2}$. If the helix is untwisted¹, the director basis can be calculated as

$$\mathbf{d}_3 = \mathbf{x}' = \frac{\kappa}{\gamma} \cos(\gamma s) \mathbf{e}_1 - \frac{\kappa}{\gamma} \sin(\gamma s) \mathbf{e}_2 + \frac{\tau}{\gamma} \mathbf{e}_3, \quad (\text{S56})$$

$$\mathbf{d}_2 = \frac{\mathbf{d}'_3}{\|\mathbf{d}'_3\|} = -\sin(\gamma s) \mathbf{e}_1 - \cos(\gamma s) \mathbf{e}_2, \quad (\text{S57})$$

$$\mathbf{d}_1 = \mathbf{d}_2 \times \mathbf{d}_3 = -\frac{\tau}{\gamma} \cos(\gamma s) \mathbf{e}_1 + \frac{\tau}{\gamma} \sin(\gamma s) \mathbf{e}_2 + \frac{\kappa}{\gamma} \mathbf{e}_3, \quad (\text{S58})$$

so that the curvature $\boldsymbol{\kappa}$ is given by

$$\boldsymbol{\kappa} = \kappa \mathbf{d}_1 + \tau \mathbf{d}_3. \quad (\text{S59})$$

Substitution of Eqns. (S59) into the equilibrium equations (S24) yields

$$F_2 = 0, \quad F'_1 = F'_3 = 0, \quad -F_3 \kappa + F_1 \tau = 0, \quad (\text{S60})$$

$$-G J \tau \kappa + E I_1 (\kappa - K) \tau + F_1 = 0. \quad (\text{S61})$$

Therefore, the force \mathbf{F} in the global coordinates can be written as

$$\mathbf{F} = F_1 \mathbf{d}_1 + F_2 \mathbf{d}_2 + F_3 \mathbf{d}_3 = \frac{F_1 \kappa + F_3 \tau}{\gamma} \mathbf{e}_3 = P \mathbf{e}_3, \quad (\text{S62})$$

indicating that there are no forces acting in the directions spanned by \mathbf{e}_1 and \mathbf{e}_2 . This is consistent with the experimental setup, where only a tensile force in the longitudinal direction

¹It has been proved that only untwisted helix can satisfy the equilibrium equations [2].

spanned by \mathbf{e}_3 is applied. Moreover, Eqns. (S60)-(S62) indicate that in an equilibrated helix the values of torsion τ , curvature κ and applied force P are related through

$$-GJ\tau\kappa + EI_1(\kappa - K)\tau + \frac{\kappa}{\gamma}P = 0. \quad (\text{S63})$$

Therefore, a helical rod satisfying Eqn. (S63) is also an equilibrium configuration. It is important to note that since in our physical experiments we only control the applied force P , Eqn. (S63) is not sufficient to determine the curvature κ and torsion τ characterizing the helical configuration. To evaluate the evolution of κ and τ as a function of the applied force P , we minimize the total energy (density) of the helix

$$\mathcal{E} = \mathcal{E}_b + \mathcal{E}_\tau + \mathcal{U}_p, \quad (\text{S64})$$

where \mathcal{E}_b , \mathcal{E}_τ and \mathcal{U}_p are the bending energy, twisting energy and force potential, respectively:

$$\mathcal{E}_b = \frac{1}{2}EI_1(\kappa - K)^2, \quad (\text{S65})$$

$$\mathcal{E}_\tau = \frac{1}{2}GJ\tau^2, \quad (\text{S66})$$

$$\mathcal{U}_p = -\frac{P}{L_*} \frac{\tau L_*}{\gamma}, \quad (\text{S67})$$

with $\tau L_*/\gamma$ being the end-to-end distance of the helix. The energy minimization criterion requires that

$$\frac{\partial \mathcal{E}}{\partial \kappa} = 0 \quad : \quad EI_1(\kappa - K) + P \frac{\kappa\tau}{\gamma^3} = 0, \quad (\text{S68})$$

$$\frac{\partial \mathcal{E}}{\partial \tau} = 0 \quad : \quad GJ\tau - P \frac{\kappa^2}{\gamma^3} = 0, \quad (\text{S69})$$

which can be solved to obtain κ and τ as a function of the applied force P . Eliminating P from Eqns. (S68) and (S69), we have

$$EI_1(\kappa - K)\kappa + GJ\tau^2 = 0, \quad (\text{S70})$$

from which we can calculate κ as

$$\kappa = \frac{1}{2}(K - Q), \quad \text{with } Q = \sqrt{K^2 - \frac{4GJ\tau^2}{EI_1}}. \quad (\text{S71})$$

Substitution of Eqn. (S71) into Eqn. (S68) yields

$$\frac{1}{2}EI_1(-K + Q) + \frac{P\tau(K + Q)}{2\left(\tau^2 + \frac{1}{4}(K + Q)^2\right)^{3/2}} = 0, \quad (\text{S72})$$

which can be solved numerically to obtain the curvature κ as a function of P .

Note that the constitutive equation (S20) indicates that a stable helix is subjected to a twisting moment $GJ\tau$ and a bending moment $EI_1(\kappa - K)$, which are not controlled in our experiments. In fact, since experimentally both ends are free to rotate, the twisting moment cannot be supported by our samples². Furthermore, we note that in a perfect helix the ends of

²Note that the bending moment is approximately supported by the non-uniform stress distribution in the bi-strip system.

the rod are not aligned. Such misalignment cannot be supported by our physical samples during the releasing process, since the gravity acts against it (see the experimental section for more details). Therefore, during the growth of the helix a transition region dominated by boundary effects near the strip ends may form and non-negligible dynamic effects may arise. Nonetheless, our experiments show that the transitional region near the ends is very short. Moreover, since the releasing process is slow, no significant dynamics effects are observed, so that Eqns. (S71)-(S72) can be used to describe the response of our system with good accuracy.

Transition from straight to helical configurations Although both straight and helical configurations represent equilibrium states for the equivalent rod, our experimental observations suggest that for large values of the applied force P the straight configuration is stable. However, when the applied force P is gradually released, the rod (a thick one) is found to evolve from a straight to a helical configuration.

Interestingly, we note that for large values of the applied force P , Eqn. (S72) does not admit a real, positive solution κ . Therefore, for large values of P helical configurations are not supported by the rod. However, a critical value of the applied force P_{cr} can be identified for which Eqn. (S72) starts to admit a real and positive solution κ . Hence, for $P < P_{cr}$ helical configurations are expected to emerge. The critical force P_{cr} can be obtained by taking the limit $\kappa \rightarrow 0$ in Eqn. (S72),

$$P_{cr} = \frac{(EI_1 K)^2}{GJ}. \quad (\text{S73})$$

Finally, to further highlight the transition from straight to helical configurations, we compare the energies of both states as a function of the applied force P . The results reported in Fig. S10 clearly show that when $P < P_{cr}$ the helix has lower energy than the straight configuration.

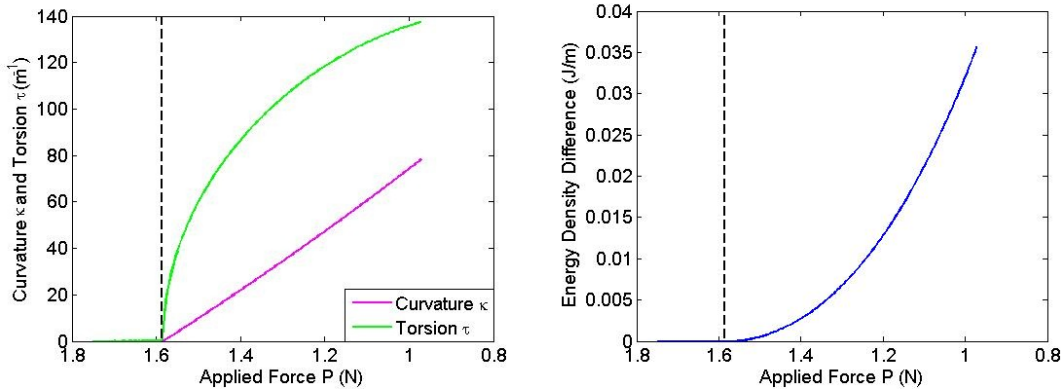


Figure S10: Left: Curvature κ and torsion τ as a function of the applied force P for a bi-strip with $\chi = 1.5$, $h = 6\text{mm}$, $w = 3\text{mm}$, $L_a = 500\text{mm}$. Note that these parameters result in a rod with $K = 0.2143\text{mm}^{-1}$ and $L_* = 331.4\text{mm}$. Right: Energy density difference $\mathcal{E}_{straight} - \mathcal{E}_{helix}$ as a function of the applied force P for the straight and helical configurations. In both plots the vertical dashed line correspond to P_{cr} .

S3.2.3 Stability of the equivalent rod

In the section above, we have proved that as the applied force P is gradually released at a critical point the straight configuration becomes unstable and the rod assumes an helical shape.

However, in the experiments during the release process we observe the formation not only of helices, but also of hemihelices with multiple reversal of chirality. Here, we show that all these complex 3D shapes can be captured conducting the general stability analysis described in Section S3.1.4. Interestingly, the analysis reveals that the helical transition studied in Section S3.2.2 can be recovered as a special case of the bifurcation branches obtained by this general stability analysis.

To understand and analyze the complex shapes observed during the release process in the pre-strained bi-strip, we start by considering a straight rod under tension, so that $\mathbf{F} = P \mathbf{d}_3$. The rod has an homogeneous rectangular cross section with edges $2w$ and h and is characterized by a length L_* and intrinsic curvature K given by (S45). In Section S3.2.2 we have shown that the straight configuration characterized by

$$(\kappa_1^{(0)}, \kappa_2^{(0)}, \kappa_3^{(0)}) = (0, 0, 0), \quad (F_1^{(0)}, F_2^{(0)}, F_3^{(0)}) = (0, 0, P), \quad (\kappa_1^{(u)}, \kappa_2^{(u)}, \kappa_3^{(u)}) = (K, 0, 0), \quad (\text{S74})$$

identically satisfies the equilibrium equations (S24). However, the experiments show that a critical tension exists for which the straight filament loses its stability and bifurcate into new solutions. To capture the bifurcation, we focus on the first order equilibrium equations (S36) and express the solution $\boldsymbol{\mu}^{(1)}$ as

$$\boldsymbol{\mu}^{(1)} = \mathbf{c} \exp(i\omega_n s), \quad (\text{S75})$$

where \mathbf{c} is the amplitude vector and $\omega_n = n\pi/L_*$ is the angular frequency of the corresponding mode. Substituting Eqns. (S74) and (S86) into (S36), the first order equilibrium equations can be rewritten as

$$\mathbf{L} \mathbf{c} = \mathbf{0}, \quad (\text{S76})$$

where \mathbf{L} is given by

$$\mathbf{L} = \begin{pmatrix} 0 & -P\omega_n^2 & 0 & -\omega_n^2 & 0 & 0 \\ P\omega_n^2 & 0 & 0 & 0 & -\omega_n^2 & 0 \\ 0 & 0 & 0 & 0 & 0 & -\omega_n^2 \\ -I_1 E \omega_n^2 & 0 & 0 & 0 & -1 & 0 \\ 0 & -I_2 E \omega_n^2 & -iEI_1 K \omega_n & 1 & 0 & 0 \\ 0 & iEI_1 K \omega_n & -GJ\omega_n^2 & 0 & 0 & 0 \end{pmatrix}. \quad (\text{S77})$$

Note that \mathbf{L} not only depends on the material properties, but also on the applied force P . In general, for large values of P the matrix \mathbf{L} is non-singular, so that only the trivial straight solution (i.e. $\mathbf{c}=\mathbf{0}$) exists. However, during the release process non-trivial solutions for $\boldsymbol{\mu}^{(1)}$ are supported when

$$\det(\mathbf{L}) = -\omega_n^2 [\omega_n^2 (P + (E\omega_n^2)I_1)] [GJ\omega_n^4 (P + E\omega_n^2 I_2) - E^2 \omega_n^4 I_1^2 K^2] = 0. \quad (\text{S78})$$

Therefore, the critical value of the applied force P_{cr} is obtained as

$$P_{cr} = \frac{(EI_1 K)^2}{GJ} - EI_2 \omega_n^2 = \frac{(EI_1 K)^2}{GJ} - EI_2 \frac{n^2 \pi^2}{L_*^2}. \quad (\text{S79})$$

Next, we construct the solution corresponding to different modes. First, we use Eqn. (S87) to calculate the eigenvector \mathbf{c} corresponding to a given pair (P_{cr}, ω_n) . Then, we substitute the solution Eqn. (S75) in Eqn. (S38) to determine the mode shape up to the first order. Moreover,

to obtain the mode shape more accurately, we solve the second order equilibrium equations (S37), where

$$\mathbf{H}_2 = \exp(2i\omega_n s) \cdot \begin{pmatrix} -2(Pc_1c_3 - 2c_3c_5 + 2c_2c_6)\omega_n^2 \\ -2(Pc_2c_3 + 2c_3c_4 - 2c_1c_6)\omega_n^2 \\ 2[P(c_1^2 + c_2^2) + 2c_2c_4 - 2c_1c_5]\omega_n^2 \\ iEI_1Kc_2^2\omega_n + iEI_1Kc_3^2\omega_n - c_3[c_4 + 2c_2(-EI_2 + GJ)\omega_n^2] \\ -iEI_1Kc_1c_2\omega_n - c_3[c_5 - 2c_1(-EI_1 + GJ)\omega_n^2] \\ c_2c_5 + c_1[c_4 - 2I_2c_2E\omega_n^2 + I_1(-iEKc_3\omega_n + 2Ec_2\omega_n^2)] \end{pmatrix}, \quad (\text{S80})$$

c_i being the i -th component of the vector \mathbf{c} determined from the first order equilibrium. The solution $\boldsymbol{\mu}^{(2)}$ can be obtained as

$$\boldsymbol{\mu}^{(2)} = \mathbf{L}^{-1} \cdot \mathbf{H}_2, \quad (\text{S81})$$

and used to determine the director basis \mathbf{d}_i up to the second order. Finally, the position vector for each bifurcation mode is obtained using Eqn. (S38) as

$$\mathbf{x} = \begin{pmatrix} \frac{GJX_n \sin(\omega_n s)}{EI_1K} \\ \frac{G^2J^2(2EI_1 + EI_2 - GJ)X_n^2\omega_n^2(\cos(2\omega_n s) - 1)}{2E^3I_1^3K^3 + 2E^2GI_1(4I_1 - I_2)JK\omega_n^2} \\ s - \frac{G^2J^2X_n^2\omega_n \sin(2\omega_n s)}{4E^2I_1^2K^2} \end{pmatrix}, \quad (\text{S82})$$

where X_n is the mode amplitude. In Fig. S11 we report the shapes of modes characterized by $n = 1, 4, 7$. The modes clearly resemble the 3D curls (hemi-helices) observed in the experiments and consist of multiple, periodic and alternating helical sections of opposite chiralities, separated by perversions. The first mode is characterized by two regions of opposite chiralities with one perversion, the second mode consists of a sequence of three regions of opposite chiralities and two perversions, the third mode consists of four regions of opposite chirality with three perversions and so on with the number of perversions monotonically increasing linearly with the mode number.

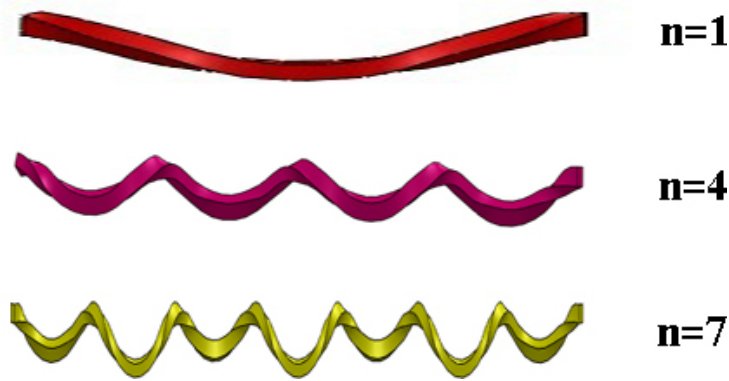


Figure S11: Reconstructions of modes characterized by $n = 1, 4, 7$.

The special case of the helix Experimental observations clearly show that for thick strips, helices and not hemihelices form during release. Here, we show that at the bifurcation onset the helix can be recovered as a special case of the hemi-helix.

In fact, at the onset of bifurcation the magnitude of both the curvature and the torsion of the helix is small, so that $\kappa \ll 1$ and $\tau \ll 1$. Substituting Eqn. (S71) into Eqns. (S55), expanding the nonlinear terms in Taylor series and retaining only first order terms, the position vector of the helix can be written as

$$\begin{aligned} x_1 &= \frac{\kappa}{\gamma^2} \sin(\gamma s) \sim \frac{GJ}{EI_1 K} \tau s + O(\tau^3) \\ x_2 &= \frac{\kappa}{\gamma^2} (\cos(\gamma s) - 1) \sim O(\tau^2) \\ x_3 &= \frac{\tau}{\gamma} s \sim s + O(\tau^2) \end{aligned} \quad (\text{S83})$$

On the other hand, if we assume that $\omega_n = n\pi/L_* \ll 1$ in Eqns. (S82), expand the nonlinear terms in Taylor series and retain only first order terms, the position vector of the hemihelix can be expressed as

$$\begin{aligned} x_1 &= -\frac{GJX_n \sin(\omega_n s)}{EI_1 K} \sim -\frac{GJ}{EI_1 K} X_n \omega_n s + O(\omega_n^3) \\ x_2 &= \frac{G^2 J^2 (2EI_1 + EI_2 - GJ) X_n^2 \omega_n^2 (\cos(2\omega_n s) - 1)}{2E^3 I_1^3 K^3 + 2E^2 G I_1 (4I_1 - I_2) JK \omega_n^2} \sim O(\omega_n^2) \\ x_3 &= s - \frac{G^2 J^2 X_n^2 \omega_n \sin(2\omega_n s)}{4E^2 I_1^2 K^2} \sim s + O(\omega_n^2) \end{aligned} \quad (\text{S84})$$

It is easy to see that Eqns. (S83) and (S84) coincide if $\tau = -X_n \omega_n$. Therefore, our analysis reveals that at the onset of bifurcation the helix can be described as an hemihelix characterized by small mode number n .

This can be further illustrated by directly comparing the mode shapes obtained using Eqns. (S82) for different values of n , as shown in Fig. S12. Since an hemi-helix consists of helical sections of opposite chiralities separated by perversions, if $n < 1$ the perversion lies outside the strip and the rod deforms into a single helical segment. Therefore, we expect to observe the formation of helices during the release process if $n < 1$.

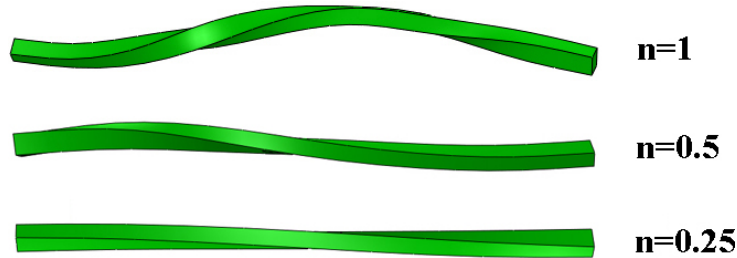


Figure S12: Reconstructions of modes characterized by $n = 1, 0.5, 0.25$. Note that for case $n = 1$, the reconstruction shows the segment between the perversions, so that the perversion lies at each end of the strip.

Finally, by taking the limit for $\omega_n \rightarrow 0$ in Eqn. (S79) we obtain

$$P_{cr} = \frac{(EI_1 K)^2}{GJ}, \quad (\text{S85})$$

which coincides with the critical force previously calculated for an helix (see Eqn. (S73)). This further confirms the close relationship between hemi-helices and helices.

S3.2.4 Mode selection

The stability analysis conducted in the previous section shows when $P \leq P_{cr}$ the straight configuration is unstable and the rod assumes a 3D shape. In Fig. S13 we report the evolution of P_{cr} as a function of the dimensionless cross-sectional parameter h/w for different modes (i.e. different values of n).

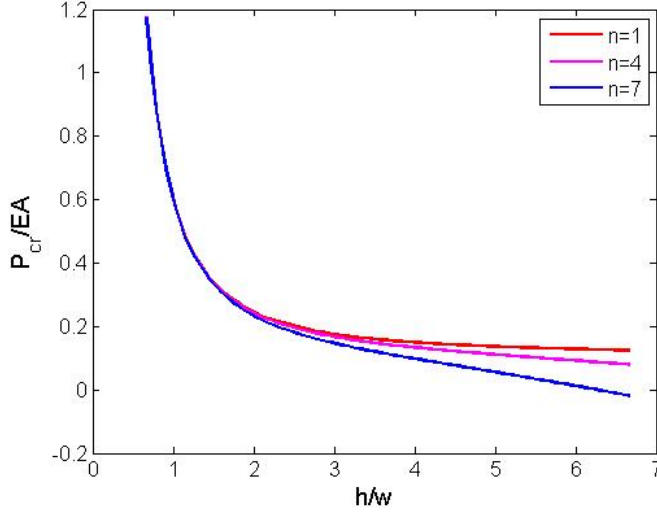


Figure S13: Critical load P_{cr} as a function of the cross-sectional aspect ratio h/w for different mode numbers n . A bi-strip characterized by $w = 3\text{mm}$, $\chi = 1.5$ and $L = 500\text{mm}$ is considered.

The results clearly show that the mode characterized by $n = 1$ is always the first to be excited. However, it is important to note that for low values of h/w the modes are closely spaced, while as h/w increases, the critical values for different modes become more and more separated. Therefore, for a thick strip low number modes are more likely to dominate, since they may evolve before higher number modes are triggered. Differently, for low values of h/w we do not expect to necessarily observe the mode with $n = 1$, but that which grows faster than the others.

Here, to determine the mode selected by the rod with a simple analysis, we assume that the fastest growing mode at the onset of the instability is the one that dominates. Although this approach neglects the contribution of geometric non-linearities and the possible interactions between different modes, it has already been successfully used to determine the mode selected by rods in a variety of contexts [5, 15, 16, 17, 18]. Moreover, we will show that the predictions obtained using this simple analysis nicely agree with both our experimental and numerical results.

Therefore, to determine the mode selected by the rod we focus on the first order equilibrium equations (S36) and express the solution $\boldsymbol{\mu}^{(1)}$ as

$$\boldsymbol{\mu}^{(1)} = \mathbf{c} \exp(\sigma t + i\omega_n s), \quad (\text{S86})$$

where σ is the growth rate of the bifurcation mode. Substituting Eqns. (S74) and (S86) into

(S36), the first order equilibrium equations can be rewritten as

$$\mathbf{L} \mathbf{c} = \mathbf{0}, \quad (\text{S87})$$

where \mathbf{L} is given by

$$\mathbf{L} = \begin{pmatrix} 0 & -A\rho\sigma^2 - P\omega_n^2 & 0 & -\omega_n^2 & 0 & 0 \\ A\rho\sigma^2 + P\omega_n^2 & 0 & 0 & 0 & -\omega_n^2 & 0 \\ 0 & 0 & 0 & 0 & 0 & -\omega_n^2 \\ -I_1(\rho\sigma^2 + E\omega_n^2) & 0 & 0 & 0 & -1 & 0 \\ 0 & -I_2(\rho\sigma^2 + E\omega_n^2) & -iEI_1K\omega_n & 1 & 0 & 0 \\ 0 & iEI_1K\omega_n & -(I_1 + I_2)\rho\sigma^2 - GJ\omega_n^2 & 0 & 0 & 0 \end{pmatrix}. \quad (\text{S88})$$

During the release process non-trivial solutions for $\boldsymbol{\mu}^{(1)}$ are supported when

$$\begin{aligned} \Delta(\sigma, \omega_n) &= \det(\mathbf{L}) = -\omega_n^2 (\rho\sigma^2 A + \omega_n^2 (P + (\rho\sigma^2 + E\omega_n^2)I_1)) \cdot \\ &((\rho\sigma^2 I_1 + \rho\sigma^2 I_2 + GJ\omega_n^2) (\rho\sigma^2 A + \omega_n^2 (P + (\rho\sigma^2 + E\omega_n^2)I_2)) - E^2\omega_n^4 I_1^2 K^2) = 0. \end{aligned} \quad (\text{S89})$$

Therefore, to determine the mode selected by the rod we calculate the growth rate σ by solving equation (S89) for a given value of P and ω_n . When $P < P_{cr}$ solutions with positive real values of σ are found, identifying perturbations that grow exponentially with time. These modes are the solutions that grow exponentially from small perturbations and are those observed in experiments. Intuitively, as a consequence of their exponential growth, we expect the modes with the highest growth rate σ to dominate the morphological evolution. In contrast, for $P > P_{cr}$ solutions with imaginary or negative σ are obtained; these will be of the order of the perturbation itself, cannot grow and hence will not be observed. Finally, when $P = P_{cr}$ we find that $\sigma = 0$ and the solution reduces to that considered in the stability analysis in Section S3.2.3.

In Fig. S14 we report the growth rate as a function of the mode number n for strips with different aspect ratio h/w . The results clearly show that the fastest growing mode in a thick strip with $h/w = 2$ is characterized by $n = 3$. Differently, for a thin strip with $h/w = 1$ the mode with $n = 9$ is the fastest to evolve and is expected to dominate. These observations nicely agree with the experimental results reported in Fig. 3 in the main text, where it is clearly shown that the mode number monotonically decreases as a function of h/w .

S3.2.5 Results and discussion

The analyses conducted in the previous sections show that during the release process a critical value of applied force P_{cr} exists below which the straight configuration is unstable. For $P < P_{cr}$ the analysis predicts the formation of hemi-helices consisting of helical sections of opposite chiralities separated by perversions. To determine the number n of perversions that form in the rod, the growth rate σ for different modes can be calculated and compared. The mode characterized by the highest growth rate σ is expected to grow faster and to dominate.

We perform a series of stability analyses on rods characterized by different values of prestrain χ and cross-sectional aspect ratio h/w and find the mode n that has the maximum growth rate σ . The results are reported in Fig. S15 as contour map. The color in the contour plot represents the associated value of n for which the growth rate is maximum and therefore correspond to the number of perversions n_p we expect to observe in the system. This parametric study reveals that the number of perversions in the rod after bifurcation is only moderately affected by the pre-strain χ , while the aspect ratio h/w is found to have a significant effect. In thin strips with $h/w \simeq 1$ the formation of 10 perversions is observed. The number of perversions n_p is then

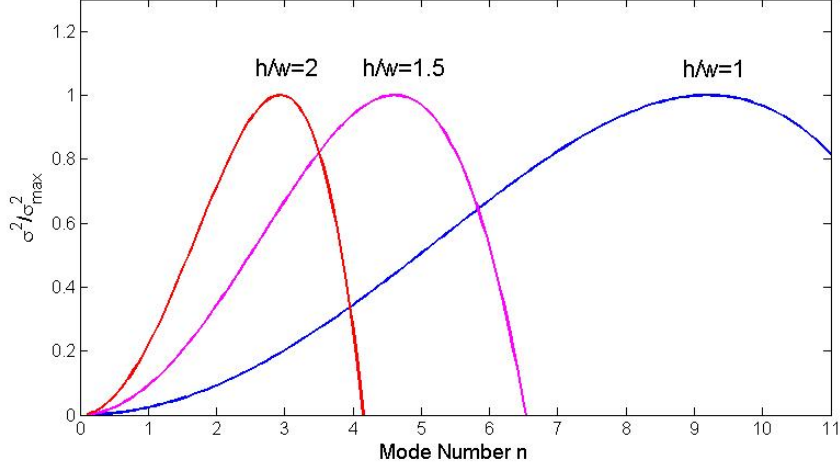


Figure S14: Growth rate σ as a function of the mode number n for three different strips characterized by $h/w = 1, 1.5, 2$, $w = 3\text{mm}$, $\chi = 1.5$ and $L = 500\text{mm}$. The growth rate is determined for an applied force $P = 0.981P_{cr}$.

found to monotonically decrease as a function of h/w . In particular, the dashed red line in the plot marks the configurations for which $n_p = 1$. As highlighted in the previous section, if $n_p < 1$ the perversion lies outside the rod, so that the system deforms into a single helical segment and the formation of helices is expected during the release process. Therefore, the red line defines the boundary between hemi-helices and helices. It is worth noting that, since the growth rate σ depends also on the applied force P , the number of perversions predicted by the analysis is also a function of P . To clarify this aspect in Fig. S16 we report the contour map for n_p calculated for different values of P . Although the value of P is found to slightly alter n_p and therefore to shift the phase boundary between hemihelices and helices, all the contour maps share the same key features.

In conclusion, the results of our analysis not only enable us to explain the evolution of the number of perversions as a function of χ and h/w observed experimentally in the bi-strip, but also, and most importantly, capture the transition from hemihelices to helices.

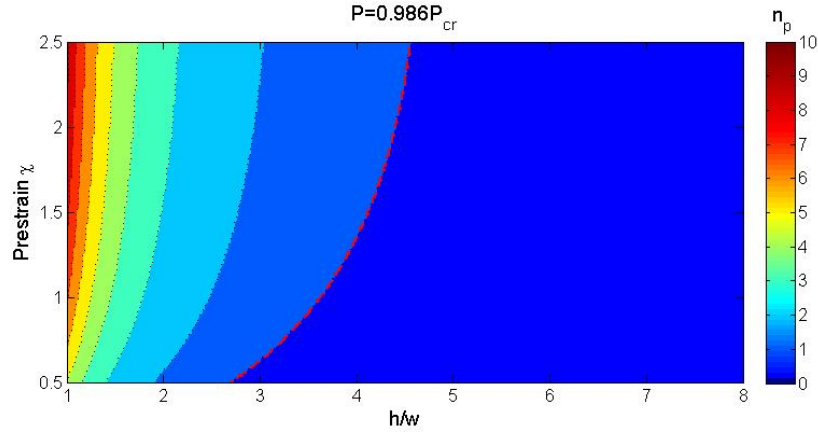


Figure S15: Contour plots showing the value of n for which the growth rate is maximum as function to χ and h/w . The growth rates are calculated for $P = 0.986P_{cr}$. Black dotted lines show the boundaries between modes with different number of perversions n_p , while the red dashed line corresponds to $n_p = 1$ and separates hemihelices (to its left) from helices (to its right).

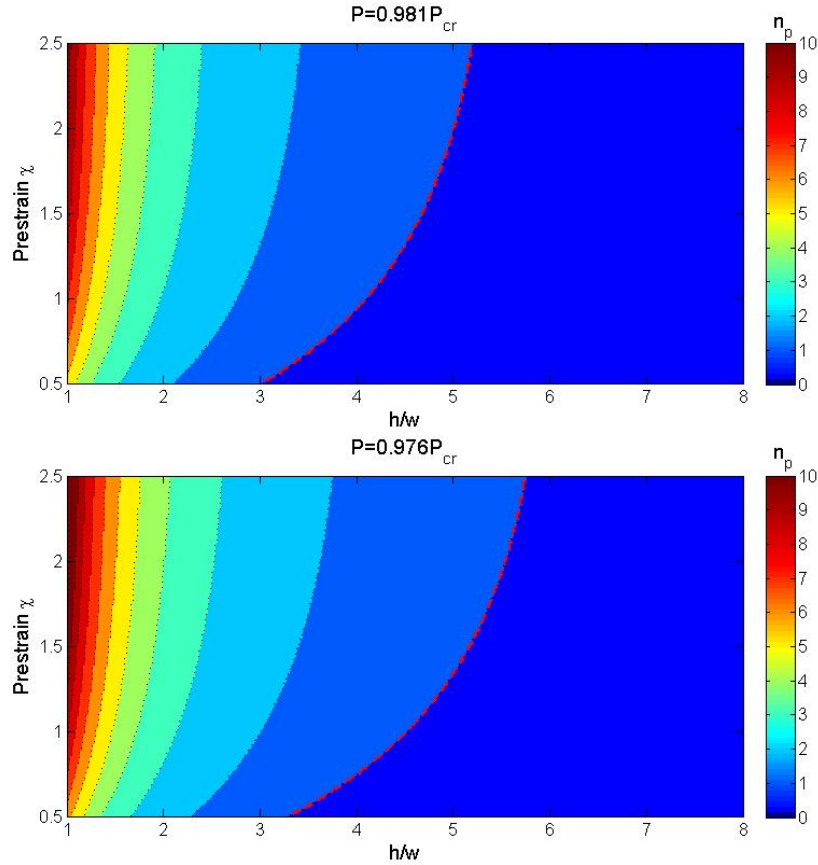


Figure S16: Contour plots showing the values of n_p for different values of applied force, $P = 0.981P_{cr}$ and $P = 0.976P_{cr}$. P is found to slightly alter the boundaries between modes characterized by different values of n_p and therefore to shift the phase boundary between hemihelices and helices. However, all the contour maps show the same key features.

References

- [1] Huang J, Liu J, Kroll B, Bertoldi K, Clarke DR (2012) Spontaneous and deterministic three-dimensional curling of pre-strained elastomeric bi-strips. *Soft Matter* 8:6291-6300.
- [2] McMillen T, Goriely A (2002) Tendril perversion in intrinsically curved rods. *J. Nonlinear Sci.* 12:241-281.
- [3] Coleman BD, Dill EH, Lembo M, Lu Z, Tobias I (1993) On the dynamics of rods in the theory of Kirchhoff and Clebsch. *Arch Rational Mech Anal* 121:339-359.
- [4] Young W, Budynas R (2002) Roark's formulas for stress & strain, 7th Edition.
- [5] Goriely A, Tabor M (1997) Nonlinear dynamics of filaments I. Dynamical instabilities. *Physica D* 105: 20-44.
- [6] Goriely A, Tabor M (1997) Nonlinear dynamics of filaments II. Nonlinear analysis. *Physica D* 105: 45-61.
- [7] Audoly B, Pomeau Y (2010) Elasticity and geometry. *Oxford University Press*.
- [8] Bower AF (2009) Applied mechanics of solids. *CRC Press. Taylor and Francis Group*.
- [9] Goriely A, Nizette M, Tabor M (2001) On the dynamics of elastic strips. *J Nonlinear Sci* 11:3-45.
- [10] Gent AN (1996) A new constitutive relation for rubber. *Rubber Chem Technol* 69:59-61.
- [11] Kroner E (1960) Allgemeine Kontinuumstheorie der Versetzungen und Eigenspannungen. *Arch Ration Mech Anal* 4:273-334.
- [12] Lee EH (1969) Elastic-Plastic deformation at finite strains. *J Appl Mech* 36:1-6.
- [13] Kirchhoff G (1859) Über das Gleichgewicht und die Bewegung eines unendlich dfinnen elastischen Stabes. *J f reine, angew Math* 56:285-313.
- [14] Kirchhoff G (1876) Vorlesungen fiber mathematische Physik. *Mechanik* 28.
- [15] Goriely A (2000) The nonlinear dynamics of filaments. *Nonlinear Dynam* 21:101-133.
- [16] Patricio P, Adda-Bedia M, Amar MB (1998) An elastica problem: instability of an elastic arch. *Physica D* 124:285-295.
- [17] Zhou H, Ou-Yang Z (1999) Spontaneous curvature-induced dynamical instability of Kirchhoff filaments: Application to DNA kink deformations. *J Chem Phys* 110:1247-1251.
- [18] Valverde J, Van der Heijden GHM (2010) Magnetically-induced buckling of a whirling conducting rod with applications to electrodynamic space tethers. *J Nonlinear Sci* 20:309-339.